

Multi-TE Single-Quantum Sodium (^{23}Na) MRI: A Clinically Translatable Technique for Separation of Mono- and Bi- T_2 Sodium Signals

Short title: Mono- and bi- T_2 sodium separation

Yongxian Qian,^{1*} Ying-Chia Lin,¹ Xingye Chen,^{1,2} Yulin Ge,¹ Yvonne W. Lui,^{1,3}
Fernando E. Boada^{1†}

¹ Bernard and Irene Schwartz Center for Biomedical Imaging, Department of Radiology, New York University Grossman School of Medicine, New York, NY 10016.

² Vilcek Institute of Graduate Biomedical Sciences, NYU Grossman School of Medicine, New York, NY 10016.

³ Department of Radiology, NYU Langone Health, New York, NY 10016.

* **Corresponding author.** Email: Yongxian.Qian@nyulangone.org

† Present address: Department of Radiology, Stanford University, Stanford, CA 94305.

Abstract (194 words)

Sodium magnetic resonance imaging (MRI) is sensitive and specific to ionic balance of cells owing to 10-fold difference in sodium concentration across membrane actively maintained by sodium-potassium ($\text{Na}^+\text{-K}^+$) pump. Disruption of the pump and/or membrane integrity, as seen in neurological disorders such as epilepsy, multiple sclerosis, bipolar disease, and mild traumatic brain injury, leads to a large increase in intracellular sodium. Such a cellular-level alteration is however overshadowed by large signal from extracellular sodium, leaving behind a long-standing pursuit to separate signals from sodium exhibiting mono- vs. bi-exponential transverse (T_2) decay under the inherent constraint of low signal-to-noise ratio even at advanced clinical field of 3 Tesla. Here we propose a novel technique that exploits intrinsic difference in their T_2 decays by simply acquiring single-quantum images at multiple echo times (TEs) and performing accurate matrix inversion at voxel. This approach was then investigated using numerical models, agar phantoms and human subjects, showing high accuracy of the separation in phantoms (95.8% for mono- T_2 and 72.5–80.4% for bi- T_2) and clinical feasibility in humans. Thus, sodium MRI at 3T can now facilitate detection of neurological disorders early at cellular level and response to treatment as well.

Acknowledgments

The authors would like to thank Dr. Ryan Brown and Mr. Karthik Lakshmanan for their support in the development of the 8-channel array sodium coil, Dr. Timothy Shepherd for his support in the recruitment of epilepsy patients, and Dr. Tiejun Zhao for his support and discussion in sodium MRI.

Funding:

National Institutes of Health (NIH) grants RF1/R01 AG067502 (YQ, YL, XC, YG, YWL, FEB), R01 NS131458 (YQ, YWL, FEB), RF1 NS110041 (YG), R01 AG077422 (YG), R01 NS113517 (YQ, FEB), R01 NS108491 (YQ, FEB), and R01 CA111996 (YQ, FEB).

Department of Radiology of the New York University Grossman School of Medicine General Research Fund (YQ, YG, YWL, FEB).

NIH-sponsor required statement:

Research reported in this publication was supported in part by the National Institute On Aging (NIA) of the National Institutes of Health (NIH) under Award Number RF1/R01AG067502. The content is solely the responsibility of the authors and does not necessarily represent the official views of the National Institutes of Health.

This work was performed under the rubric of the Center for Advanced Imaging Innovation and Research (CAI²R), a National Institute of Biomedical Imaging and Bioengineering (NIBIB) Biomedical Technology Resource Center grant NIH P41 EB017183.

Author contributions:

Conceptualization: YQ, FEB

Methodology: YQ, YWL, FEB

Investigation: YQ, YL, XC, YG, YWL, FEB

Visualization: YQ, YWL, FEB

Supervision: FEB

Writing – original draft: YQ

Writing – review & editing: YQ, YL, XC, YG, YWL, FEB

Competing interests:

YQ and FEB are inventor of the U.S. Patent Application, No.: 63/591,751. Title: *Process of multiple echo time acquisitions for quantitative bi- T_2 sodium magnetic resonance imaging*. Filed on October 19, 2023. IP Owner: New York University.

All other authors declare they have no competing interests.

This work was partially presented in the 25th Annual Meeting of ISMRM 2017, Honolulu, Hawaii, USA.

This work was presented in a different version on the preprint platform arXiv.com (<https://arxiv.org/abs/2407.09868>).

Data and materials availability:

Upon written request to the corresponding author, Yongxian Qian, PhD, all data (sodium images and FID signals) and codes used in this work (main text and supplementary materials) are available to any researcher solely for scientific research purposes.

Introduction (741 words)

In human brains, sodium ions (Na^+), when exposed to an electric field gradient of negatively charged macromolecules and proteins, experience nuclear quadrupolar interaction that results in bi-exponential decay in transverse (T_2) relaxation of nuclear spins when ions are not in fast motion – a situation in which correlation time between sodium ions and electric field gradient is much shorter than the inverse of Larmor frequency, $\tau_c \ll 1/\omega_0$ (1, 2). On the other hand, sodium ions in relatively fast motion cancel out the effect of quadrupolar interactions, resulting in mono-exponential T_2 decay (1–4). Historically, short- T_2 component of the bi- T_2 decay was mis-considered arising from “bound” sodium (5, 6) as it was not detectable by then-NMR (nuclear magnetic resonance) (1–4). The terminology of “bound sodium” however remains in use in today’s literature of sodium MRI, but it comes into question more recently (7). For clarity, this article refers to “bi- T_2 ” sodium as those showing bi-exponential T_2 decay and “mono- T_2 ” sodium as those showing mono-exponential T_2 decay. Of note, mono- and bi- T_2 sodium ions can appear in both intra- and extracellular spaces (8–10), dependent on relative correlation time with electric field gradient (1, 2).

Sodium (^{23}Na) MRI (magnetic resonance imaging) currently acquires signals from both mono- and bi- T_2 sodium ions, and quantifies total sodium concentration (TSC) at voxels of an image. TSC is unique measure for non-invasive assessment of disruption in ionic homeostasis of cells in, or recovery from, pathological conditions including stroke, tumor, multiple sclerosis, epilepsy, bipolar disorder, and mild traumatic brain injury (8–12). However, TSC is dominated by mono- T_2 sodium in cerebrospinal fluid (CSF) which has a high sodium concentration (~145 mM) and overshadows alteration in intracellular sodium which has a much lower concentration (~15 mM). Separation of mono- and bi- T_2 sodium signals can remove CSF impact and highlight intracellular alterations, especially at early stage of a disease happening at cellular level or in early (cellular) response to a treatment.

The difference in T_2 relaxation was extensively explored in sodium MRI as a means to separate the two populations of sodium ions in the brain. Triple quantum filtering (TQF) was considered a standard for human studies, in which magnetic resonance (MR) signals were generated solely from triple-quantum (TQ) transitions (13). TQF techniques however require multiple radiofrequency (RF) pulses for excitation and multi-step phase cycling to eliminate single-quantum (SQ) signals (13–17), leading to long scan time (20–40 min) and high specific absorption rate (SAR) causing a safety concern. More problematic is that TQF has much low signal-to-noise ratio (SNR) about 10 folds lower than SQ (15–17). These difficulties hamper TQF to be widely used on humans.

Alternative approaches were proposed. Inversion recovery (IR), adopted from proton (^1H) MRI, exploits a difference in longitudinal (T_1) relaxation between mono- and bi- T_2 sodium ions, and suppresses signals from mono- T_2 sodium of longer T_1 time (18–20). IR approach needs an extra RF pulse for the suppression and worsens SAR issue, unfavorable to human studies (20, 21). It also suffers from incomplete suppression of mono- T_2 sodium signals which are ~ 10 folds higher than bi- T_2 sodium signals, due to spatial inhomogeneity of B_1^+ field although adiabatic pulses are usually used, and complicates quantification of bi- T_2 sodium owing to unknown residual mono- T_2 sodium signals (9,11,18). To overcome these drawbacks, another alternative approach, called short- T_2 imaging, was proposed in which SQ images were acquired at multiple echo times (TEs) and then subtracted from each other to produce an image of the short- T_2 component of bi- T_2 sodium (22–25). In such a way, SAR was reduced to, and SNR was increased to, the level of SQ images, favorable to human studies in clinic. Unfortunately, the subtraction could not completely eliminate mono- T_2 sodium signal ($\sim 20\%$ in residual), degrading accuracy of bi- T_2 sodium quantification (25).

In this study, the concept of short- T_2 imaging is generalized to multi-TE single-quantum (MSQ) imaging with a more accurate matrix inversion replacing the subtraction to substantially improve accuracy of the separation between mono- and bi- T_2 sodium signals. To develop MSQ technique, we optimized TEs for data acquisition, investigated impact of T_2 values on accuracy of the separation, and acquired free induction decay (FID) signals to generate T_2^* spectrum for the matrix equation. To test MSQ technique, we implemented numerical simulations, phantom experiments, and human studies. The results are supportive of the proposed MSQ technique. We also itemized limitations of the MSQ technique and potential pitfalls in interpretation of the separated sodium signals.

Results (1,518 words)

Model of sodium MRI signals

A two-population model, Eq. (1), is used to describe single-quantum sodium image signal, $m(t)$, evolving with time t at an imaging voxel ΔV . Time $t = 0$ is at the center of excitation RF pulse.

$$m(t) = m_{mo} Y_{mo}(t) + m_{bi} Y_{bi}(t), \quad t \geq 0 \quad (1)$$

$$\text{With } m_{mo} \geq 0, m_{bi} \geq 0, \text{ and } m_{mo} + m_{bi} = m(0)$$

$$Y_{mo}(t) \equiv \exp(-t/T_{2,mo}) \quad (1A)$$

$$Y_{bi}(t) \equiv a_{bs} \exp(-t/T_{2,bs}) + a_{bl} \exp(-t/T_{2,bl}) \quad (1B)$$

The m_{mo} and m_{bi} are signal intensity proportional to volume fraction v_q and sodium concentration C_q , i.e., $m_q \propto \Delta V v_q C_q$, $q=mo$ and bi , for mono-T₂ and bi-T₂ sodium populations in a voxel ΔV , respectively. $Y_{mo}(t)$ is relaxation decay of the mono-T₂ sodium of time constant $T_{2,mo}$ while $Y_{bi}(t)$ for the bi-T₂ sodium with $a_{bs} = 0.6$ for the short-T₂ component $T_{2,bs}$, and $a_{bl} = 0.4$ for the long-T₂ component $T_{2,bl}$. The split of 60:40 % in intensity of bi-T₂ sodium is from theoretical and experimental results for individual sodium nuclear spins (1–4, 26). These T₂ values are in an order of $T_{2,bs} \ll T_{2,bl} \leq T_{2,mo}$. However, Eq. (1) doesn't include mono-T₂ sodium of short T₂ value.

Separation of mono- and bi-T₂ sodium signals

Given SQ sodium images at multiple echo times, $TEs = \{TE_1, TE_2, \dots, TE_N\}$, in which TE is defined as time interval between the center of excitation RF pulse and center of the k -space, Eq. (1) becomes a matrix equation Eq. (2).

$$\mathbf{M} = \mathbf{Y} \mathbf{X} \quad (2)$$

$$\mathbf{M} \equiv (m_1, m_2, \dots, m_N)^T, \quad m_i = m(TE_i), i = 1, 2, \dots, N \quad (2A)$$

$$\mathbf{X} \equiv (m_{mo}, m_{bi})^T \quad (2B)$$

$$\mathbf{Y} \equiv \begin{pmatrix} Y_{mo}(TE_1) & Y_{bi}(TE_1) \\ Y_{mo}(TE_2) & Y_{bi}(TE_2) \\ \vdots & \vdots \\ Y_{mo}(TE_N) & Y_{bi}(TE_N) \end{pmatrix} \quad (2C)$$

Superscript T is operator for matrix transpose. A solution to Eq. (2) is given in Eq. (3) via an established algorithm called non-negative least-squares (NNLS) (27) in which the non-negative condition on \mathbf{X} is incorporated into the solution.

$$\mathbf{X} = NNLS(\mathbf{Y}\mathbf{X} - \mathbf{M}) \quad (3)$$

Flowchart of the MSQ approach

The proposed MSQ approach is illustrated in Fig. 1. The inputs are multi-TE sodium images and an FID signal. The outputs are mono-T₂, bi-T₂, and total sodium images, as well as maps of field inhomogeneity ΔB_0 and single-term exponential fitted effective T₂ (called T₂^{*}) – single-T₂^{*} for short. Hereinafter, T₂^{*} replaces T₂ as spin echo is not favorable to sodium MRI. Motion correction (MoCo) across multi-TE images is optional. Also optional is the low-pass (LP) filtering, which is a 3D averaging over a size of 3×3×3 voxels for instance, to reduce random noise on the bi-T₂ sodium images. The ΔB_0 and single-T₂^{*} maps present spatial distributions of the B_0 field inhomogeneity and the short- and long-T₂^{*} components, providing indications for uncertain short-

T_2^* decays possibly caused by B_0 inhomogeneity. Such maps are complimentary but critical to quantification and interpretation of the separated mono- and bi- T_2 sodium signals.

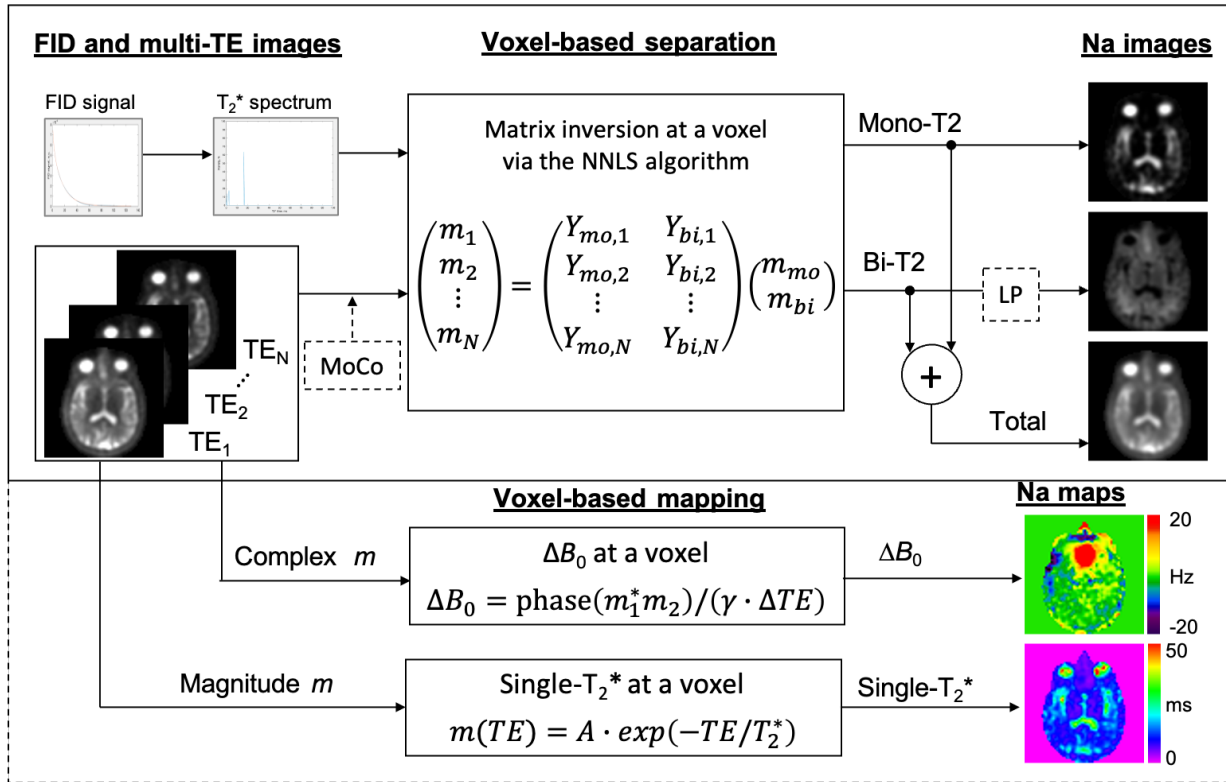


Fig. 1. Flowchart of the proposed MSQ sodium MRI. Input: multi-TE SQ images $m(TE)$ and an FID signal producing T_2^* spectrum. Motion correction (MoCo) between SQ images is optional. **Separation:** matrix inversion voxel-by-voxel across field-of-view (FOV). **Output:** three sodium images (mono- T_2 as m_{mo} , bi- T_2 as m_{bi} , and total as $m_{mo}+m_{bi}$). The low-pass (LP) filtering (optional) is a 3D smoothing of size $3 \times 3 \times 3$ or others, to further reduce random noise. **Additional outputs:** the maps of B_0 inhomogeneity and single- T_2^* .

Human studies

To demonstrate feasibility of the proposed MSQ approach at clinical field strength of 3 Tesla, we conducted the human study on 15 subjects including nine healthy adults (age 39.6 ± 21.4 years ranging 21–74 years; 3 males and 6 females) and six patients with diverse neurological conditions (1 bipolar disorder, 3 epilepsy, 1 multiple sclerosis, and 1 mild traumatic brain injury; age 30.5 ± 15.1 years ranging 18–59 years; 3 males and 3 females), after the exclusion of one healthy subject and one patient due to motion between the two TE-images. The MSQ sodium MRI was performed on a clinical 3T MRI scanner (Prisma, Siemens Healthineers, Erlangen, Germany) with a custom-built 8-channel dual-tuned (^1H - ^{23}Na) head array coil (32).

Fig. 2 presents a typical case from a young healthy female of age 26 years and includes 3D sodium images of the brain at $TE_1/TE_2=0.3/5\text{ms}$ (Fig. 2A), FID signal of whole brain and associated fitting error and T_2^* spectrum (Fig. 2B), the separated sodium images from the two-TE images using $(T_{2,mo}^*, T_{2,bs}^*, T_{2,bl}^*) = (50.0, 6.0, 19.0)$ ms (Fig. 2C), and inverse-contrast displays (Fig. 2D). In Figs. 2E-G are SNR, ΔB_0 , and single- T_2^* maps calculated from the two-TE images in Fig. 2A. Fig. 2 indicates that signals from CSF in the brain were effectively separated into mono- T_2 sodium image (Fig. 2C or 2D), while signals from brain tissues such as gray and white matters were separated into bi- T_2 sodium image (Fig. 2C or 2D). Notably and surprisingly, signal intensity across brain tissues looks more uniform in the bi- T_2 sodium images than in the mono- T_2 sodium images (Fig. 2C), total sodium images (Fig. 2C), and TE_1 -images (Fig. 2A). SNR in Fig. 2E is ≥ 25 in most regions of the brain, ensuring a robust separation as suggested in the simulations in Extended Data (Fig. E4). The field inhomogeneity ΔB_0 in Fig. 2F varied between ± 20 Hz across the brain, with the largest off-resonance in the prefrontal and occipital lobes, leading to visible blurring of the tissues in the bi- T_2 sodium images (Fig. 2C or 2D, sagittal). The single- T_2^* map in Fig. 2G provides a spatial distribution of short and long T_2^* components across the brain, complementary to T_2^*

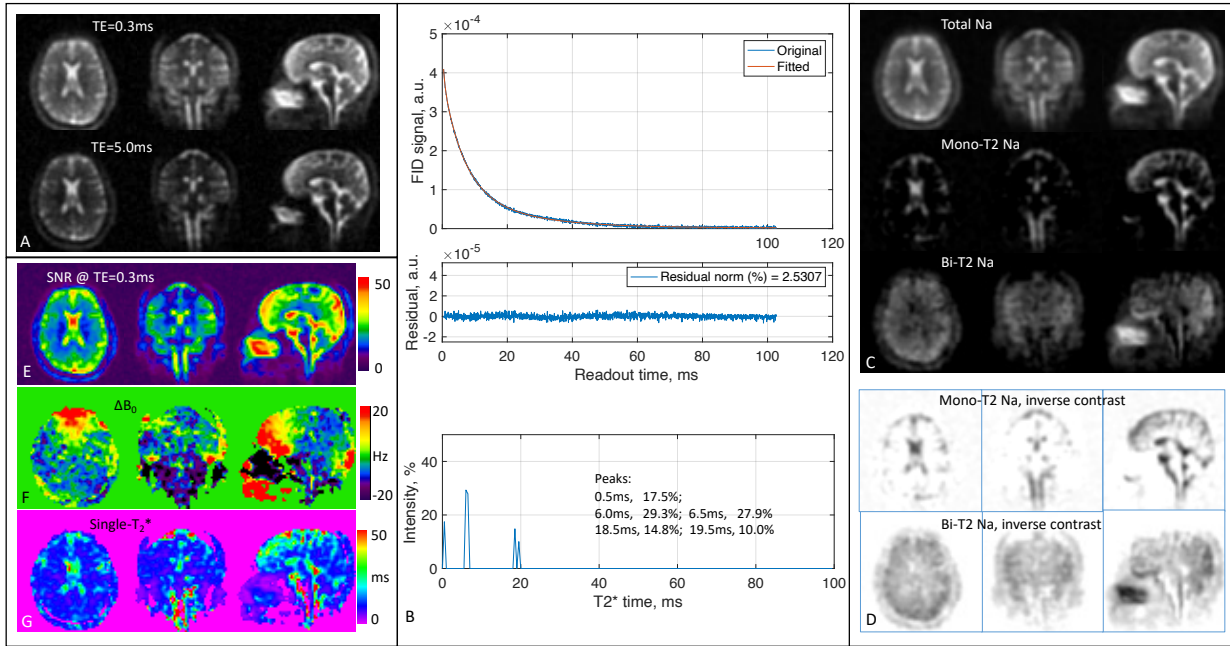


Fig. 2. Human study #1 (26-year-old female, healthy). (A) 3D sodium images of the brain in three orthogonal slices at $TE_1/TE_2=0.3/5\text{ms}$. (B) FID signal of whole brain and associated fitting error and T_2^* spectrum. (C) Separated sodium images from the 2-TE images in A using $(T_{2,mo}^*, T_{2,bs}^*, T_{2,bl}^*) = (50.0, 6.0, 19.0)$ ms according to peaks in B. (D) Inverse-contrast display to highlight areas of low intensity. All the images in A and C were displayed using the same window/level. (E-G) Maps of SNR, ΔB_0 , and single- T_2^* , calculated from the 2-TE images in A.

spectrum in Fig. 2B. It also indicates that majority of long T_2^* components are located in the prefrontal lobe in this particular case (Fig. 2G, sagittal).

Fig. 3 shows potential benefits from bi- T_2 sodium images of patients with neurological disorders such as bipolar disorder which is known to cause abnormally-high intracellular sodium concentration in the brain but locations are hard to define (33, 34). This case reports a middle-aged male patient of age 59 years with self-reported bipolar disorder. The separated sodium images were attained at $(T_{2,mo}^*, T_{2,bs}^*, T_{2,bl}^*) = (50.0, 2.5, 7.0)$ ms according to the peaks in Fig. 3B. The bi- T_2 sodium images (Fig. 3C or 3D) clearly highlighted brain regions of an elevated bi- T_2 sodium signal against surrounding tissues, with a ratio of 1.78 vs. 1.40 (or 27.1% increase) before the separation (Fig. 3C). These regions have no visible contrast in total or TE_1 -images (Fig. 3A or 3C). SNR in these regions is >40 (Fig. 3E), supporting a robust separation. The field inhomogeneity ΔB_0 in these regions is low (<5 Hz, Fig. 3F), excluding field-induced artifacts. Single- T_2^* map in Fig. 3G shows abnormally low T_2^* values in the regions, confirming an increase in short- T_2^* components.

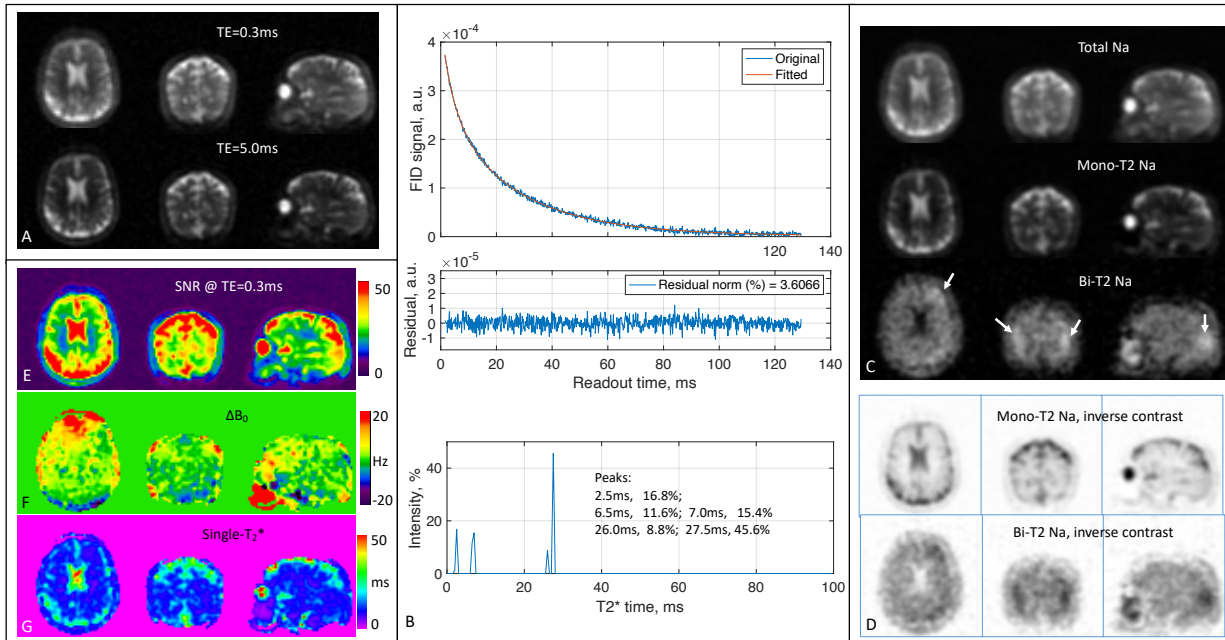


Fig. 3. Human study #2 (59-year-old male, bipolar disorder patient). (A) 3D sodium images of the brain at $TE_1/TE_2=0.3/5$ ms. (B) FID signal of whole brain and associated fitting error and T_2^* spectrum. (C) Separated sodium images from the 2-TE images in A using $(T_{2,mo}^*, T_{2,bs}^*, T_{2,bl}^*) = (50.0, 2.5, 7.0)$ ms according to peaks in B. (D) Inverse-contrast display to highlight areas of low intensity. All the images in A and C were displayed using the same window/level, except bi- T_2 sodium where W/L was halved. (E-G) Maps of SNR, ΔB_0 , and single- T_2^* , calculated from the 2-TE images in A. Note that the bi- T_2 sodium images in C highlight possible regions (arrows) of elevated bi- T_2 sodium concentration in the parenchyma.

Discussion (510 words)

We presented here a new technique MSQ to separate mono- and bi- T_2 sodium signals with high accuracy offered by matrix inversion voxel by voxel (Fig. 1). The MSQ approach leverages intrinsic difference in T_2 relaxation between the two sodium populations (Figs. 2, 3). The 2-TE sampling scheme stands out for smaller noise transfer during the separation (Extended Data Fig. E3). The T_2^* spectrum of whole brain has sparse peaks and confirms a global set of T_2^* values $\{T_{2,mo}^*, T_{2,bs}^*, T_{2,bl}^*\}$ applicable to humans (Extended Data Fig. E1). The measurement of T_2^* spectrum facilitates fine tuning of the global set of T_2^* values towards individual subjects of diverse T_2^* relaxations in the brain (Figs. 2, 3).

However, a global set of T_2^* values may not be plausible in such situations where T_2^* in an individual brain has substantial spatial variation (37–44), multi-regional sets, or a linear combination of them, may be applied to the separation.

Of note, subsequent quantification of sodium concentrations after the separation is not addressed in this study because such quantification involves complicated procedures including calibration to sodium concentration from signal and corrections for inhomogeneous coil sensitivity. These procedures deserve a separate study to adequately address in detail.

The MSQ approach has limitations and understanding them is crucial to practice of the approach. The first limitation is the two-population model (mono- and bi- T_2) which is of risk to produce a false-positive error for bi- T_2 sodium. For instance, if there is no bi- T_2 but rather two mono- T_2 sodium decays of different T_2^* values within a voxel, they would be falsely separated into bi- T_2 sodium because they can be combined mathematically into a bi-exponential decay. This kind of false positive error stems from the fact that the separation is based on *mathematical* model, instead of *physical* model as does the TQF separation.

The second limitation may occur at voxels filled solely with mono- T_2 sodium of very small T_2^* value, such as regions in nose and sinuses (Figs. 2C and 3C). Such areas may mislead the MSQ to produce pseudo bi- T_2 sodium. These mis-separated regions can be readily identified by cross-referencing the maps of ΔB_0 and single- T_2^* (Figs. 2 and 3).

The third limitation is the underestimate of bi- T_2 sodium signal caused by the image at TE_1 , as illustrated in the phantom studies (Extended Data Fig. E5). The separation Eq. (2) assumes TE_1 -image intensity precisely at TE_1 (i.e., a very short readout time). Actual TE_1 -image intensity is an average over readout time during which short- T_2^* components decay significantly when readout is relatively long, such as readout time $T_s=36.32\text{ms}$ about ten times long of a short- T_2^* of 3ms seen in this study. Therefore, the extent of underestimation depends on readout time or pulse sequence.

To mitigate this problem, two strategies may be applicable. One is to replace TE_1 in Eq. (2) with an effective (larger) value accounting for short- T_2^* decay during readout. The other is to shift $T_{2,bs}^*$ to a larger value, as did in previous work on phantoms (30). Alternatively, correction for such underestimation may be integrated into calibration process when calculating sodium concentration (Extended Data Fig. E5).

Materials and methods (955 words)

Experimental Design

The objective of this study is to demonstrate the feasibility of proposed MSQ approach to separation of mono- and bi- T_2 sodium signals from human brains at a clinical field strength of 3 Tesla. We designed three types of experiments: numerical simulations, phantom experiments, and human subject studies. To implement the MSQ approach, we used a clinical MRI scanner at 3 Tesla for data acquisition and a custom-developed software package for data processing.

Clinical MRI scanner for data acquisition

The sodium MRI images and FID signals were acquired on two 3T clinical MRI scanners for the phantom experiments and human studies, respectively. One was MAGNETOM Trio Tim (Siemens Medical Solutions, Erlangen, Germany) with a dual-tuned (1H - ^{23}Na) volume head coil (Advanced Imaging Research, Cleveland, OH), and used for the phantom experiments. The other was MAGNETOM Prisma (Siemens Healthineers, Erlangen, Germany) with a custom-built 8-channel dual-tuned (1H - ^{23}Na) head array coil (32), and used for human studies.

Software for data processing and image display

We developed a software (code) called *SepMoBi* in MATLAB (R2021a, MathWorks, Natick, MA) on a laptop computer (MacBook Pro, 16GB memory, Apple M1 chip, Apple Inc., Cupertino, CA), and used it for data processing, including the calculations of T_2^* spectrum, mono- and bi- T_2 sodium images, and maps of SNR, ΔB_0 and single- T_2^* . In addition, we used software *MRView* (MRI Research, Mayo Clinic and Foundation, December, 2020) for image display and parameter calculation in ROIs (Extended Data Fig. E6).

Pre-processing of FID signals

When acquired with an array coil, FID signals may have unique initial phases $\{\varphi_{0,l}, l=1, 2, \dots, N_c\}$ at individual elements, and need to be aligned to produce a resultant FID signal. Alignment (via

phase correction) can be towards a reference phase such as zero phase, one of the initial phases, or mean phase across elements. In addition, signal intensity at individual elements needs to be scaled using “FFT factor” stored in the header of a raw FID data file, for instance.

FID signals at the first few samples are distorted by hardware filtering during analog-to-digital conversion (ADC). The number of affected samples are in a range of 3–10 points, dependent on sampling bandwidth, with the first sample having the largest distortion. This distortion alters measurement of T_2^* components, especially the short T_2^* components which are critically important to the bi- T_2 sodium. Correction for the distortion can be performed using an established exponential extrapolation (see Supporting Materials).

Global T_2^* spectrum

We measured FID signals on clinical 3T MRI scanners using a product pulse sequence, either *AdjXFre* embedded in manual shimming or independent *fid_23Na*, with acquisition parameters: TE=0.35–1.0ms, TR=100–300ms, and averages =1–128, and TA=0.2–39s. After the pre-processing described above, resultant FID signals are curve-fitted to Eq. (4) using the NNLS algorithm (27) when T_2^* values are pre-distributed in a range of interest [$T_{2,\min}^*$, $T_{2,\max}^*$] at uniform or non-uniform intervals $\{\Delta T_{2,j}^*, j = 1, 2, \dots\}$. Amplitudes $\{A_j\}$, called T_2^* spectrum, determine relative incidence of T_2^* components in an imaging volume which counts all T_2^* components from both mono- and bi- T_2 sodium populations. We used a uniform interval of $\Delta T_2^* = 0.5\text{ms}$ in a range of interest 0.5–100 ms for a high resolution of T_2^* values. Assignment of the peaks in the T_2^* spectrum to $\{T_{2,mo}^*, T_{2,bs}^*, T_{2,bl}^*\}$ was based on their relative positions of $T_{2,mo}^* \geq T_{2,bl}^* \gg T_{2,bs}^*$ and intensity ratio about 6:4 for the bi- T_2 sodium. Robustness of the T_2^* measurement including data acquisition and spectrum computation is addressed in Supporting Information.

Human studies

The human studies were approved by local Institutional Review Board (IRB) at NYU Grossman School of Medicine, New York, NY, USA, and performed in accordance with relevant guidelines and regulations. Informed consent was obtained from all subjects. For data acquisition, the same TPI pulse sequence was used as in the phantom studies. Sodium images were reconstructed off-line using the gridding algorithm (47, 48), channel by channel, and combined into a resultant image via the sum-of-squares (SOS) algorithm (49). To decouple random noise across channels, an orthogonal linear transform (detailed in Ref. 46) was performed in which physical channel data were transformed into virtual channels with random noise independent from channel to channel. This

decoupling and denoising process also normalized signal amplitudes across channels by dividing noise standard deviation. Separation of the mono- and bi- T_2 sodium signals was then implemented in the same way as in the phantom studies.

Mapping of ΔB_0 and single- T_2^*

To map ΔB_0 or Δf_0 ($=\gamma\Delta B_0/2\pi$), Hermitian product method (50) was performed via Eqs. (10–12) at individual imaging voxels to calculate phase differences $\{\Delta\varphi_i, i = 1, 2, \dots, N - 1\}$ between TEs $\{TE_i, i = 1, 2, \dots, N\}$. Image amplitude at individual channels were corrected with the scale factors $\{w_l, l = 1, 2, \dots, N_c\}$. Phase unwrapping was not performed due to small intervals in the TEs and, in general, small inhomogeneity in B_0 field in sodium MRI. Computation for ΔB_0 map is fast (0.078s) on a Mac laptop computer for images of matrix size $64 \times 64 \times 64$ at two TEs.

$$\Delta f_0 = \frac{1}{2\pi(N-1)} \sum_{i=1}^{N-1} \Delta\varphi_i / \Delta TE_i \quad (10)$$

$$\Delta\varphi_i = \text{phase}\{\sum_{l=1}^{N_c} w_l^2 \cdot m_l^*(TE_i) \cdot m_l(TE_{i+1})\} \quad (11)$$

$$\Delta TE_i = TE_{i+1} - TE_i \quad (12)$$

To map single- T_2^* , a MATLAB curve-fitting function $\text{fit}(x, y, 'exp1')$ was used to calculate single- T_2^* values at each voxel via Eq. (13). A restriction ($T_2^*_{\max} < 100\text{ms}$) was enforced to exclude unreasonable values caused by random noise. The computation time is acceptable (10min17s).

$$|m(TE_i)| = A_0 \exp(-TE_i/T_2^*), \quad 0 \leq T_2^* \leq T_{2,\max}^* \quad (13)$$

Calculation of signal-to-noise ratio (SNR)

In a region of interest (ROI), SNR was calculated via Eq. (14) in a simplified way for both volume and array coils by taking the ratio of mean intensity S in a ROI to noise standard deviation (SD) in noise-only background regions. A factor of 0.655 was applied to noise SD to account for Rician distribution in magnitude images (51). For SNR mapping, pixel signal is used in the calculation.

$$SNR = 0.655 S / SD \quad (14)$$

Statistical Analysis

A regular statistical significance ($P=0.05$) was applied to the comparisons, via Student's t -test, between the two sets of data in this work. Minimum sample size for the t -test is 16, with 80% power, 5% significance level, two-sided test, and 1.0 effect size (29).

References

1. P. S. Hubbard, Nonexponential nuclear magnetic relaxation by quadrupole interaction. *J. Chem. Phys.* **53**, 985-987 (1970).
2. G. Jaccard, S. Wimperis, G. Bodenhausen, Multiple-quantum NMR spectroscopy of $S=3/2$ spins in isotropic phase: A new probe for multiexponential relaxation. *J. Chem. Phys.* **85**, 6282-6293 (1986).
3. M. Shporer, M. M. Civan, Nuclear magnetic resonance of sodium-23 linoleate-water: Basis for an alternative interpretation of sodium-23 spectra within cells. *Biophys. J.* **12**, 114-122 (1972).
4. J. Andrasko, Nonexponential relaxation of $^{23}\text{Na}^+$ in agarose gels. *J. Magn Reson.* **16**, 502-504 (1974).
5. F. Cope, NMR evidence for complexing of Na^+ in muscle, kidney, and brain, and by actomyosin. The relation of cellular complexing of Na^+ to water structure and to transport kinetics. *J. Gen. Physiol.* **50**, 1353-1375 (1967).
6. H. Sterk, H. Schrunner, On the discrimination of bound and mono-T2 sodium ions in solutions of biomolecules by means of the T1 relaxation. *J. Mol. Liq.* **30**, 1781-183 (1985).
7. D. Burstein, C. S. Springer Jr., Sodium MRI revisited. *Magn. Reson. Med.* **82**, 521-524 (2019).
8. S. S. Winkler, Sodium-23 magnetic resonance brain imaging. *Neuroradiology.* **32**, 416-420 (1990).
9. S. K. Hilal, A. A. Maudsley, J. B. Ra, H. E. Simon, P. Roschmann, S. Wittekoek, Z. H. Cho, S. K. Mun, In vivo NMR imaging of sodium-23 in the human head. *J. Comput. Assist. Tomogr.* **9**, 1-7 (1985).
10. W. H. Perman, P. A. Turski, L. W. Houston, G. H. Glover, C. E. Hayes, Methodology of in vivo human sodium MR imaging at 1.5 T. *Radiology.* **160**, 811-820. (1986).
11. K. R. Thulborn, Quantitative sodium MR imaging: A review of its evolving role in medicine. *NeuroImage.* **168**, 250-268 (2018).
12. P. A. Bottomley, Sodium MRI in man: technique and findings. *eMagRes.* **1**, 353-365 (2012).
13. C. Chung, S. Wimperis, Optimum detection of spin-3/2 biexponential relaxation using multiple-quantum filtration techniques. *J. Magn. Reson.* **88**, 440-447 (1990).
14. G. Navon, Complete elimination of the extracellular ^{23}Na NMR signal in triple quantum filtered spectra of rat heart in the presence of shift reagents. *Magn. Reson. Med.* **30**, 503-506 (1993).

15. R. Reddy, M. Shinnar, Z. Wang, J. S. Leigh, Multiple-quantum filters of spin-3/2 with pulses of arbitrary flip angle. *J. Magn. Reson.* **104**,148-152 (1994).
16. I. Hancu, F. E. Boada, G. X. Shen, Three-dimensional triple-quantum-filtered ^{23}Na imaging of in vivo human brain. *Magn. Reson. Med.* **42**, 1146-1154 (1999).
17. A. Tsang, R. W. Stobbe, C. Beaulieu, Triple-quantum-filtered sodium imaging of the human brain at 4.7T. *Magn. Reson. Med.* **67**, 1633-1643 (2012).
18. R. Stobbe, C. Beaulieu. In vivo sodium magnetic resonance imaging of the human brain using soft inversion recovery fluid attenuation. *Magn. Reson. Med.* **54**, 1305-1310 (2005).
19. P. Rong, R. R. Regatte, A. Jerschow, Clean demarcation of cartilage tissue ^{23}Na by inversion recovery. *J. Magn. Reson.* **193**, 207-209 (2008).
20. A. B. Mennecke, A. M. Nagel, K. Huhn, R. A. Linker, M. Schmidt, V. Rothhammer, T. Wilferth, P. Linz, J. Wegmann, F. Eisenhut, T. Engelhorn, Longitudinal sodium MRI of multiple sclerosis lesions: Is there added value of sodium inversion recovery MRI. *J. Magn. Reson. Imaging.* **55**, 140-151 (2022).
21. T. Okada, T. Akasaka, Editorial for “Longitudinal Sodium MRI of Multiple Sclerosis Lesions: Is There Added Value of Sodium Inversion Recovery MRI?”. *J. Magn. Reson. Imaging.* **55**, 152-153 (2022).
22. J. B. Ra, S. K. Hilal, Z. H. Cho, A method for in vivo MR imaging of the short T2 component of sodium-23. *Magn. Reson. Med.* **3**, 296-302 (1986).
23. J. B. Ra, S. K. Hilal, C. H. Oh, An algorithm for MR imaging of the short T2 fraction of sodium using the FID signal. *J. Comput. Assist. Tomogr.* **13**, 302-309 (1989).
24. N. Benkhedah, P. Bachert, A. M. Nagel, Two-pulse biexponential weighted ^{23}Na imaging. *J. Magn. Reson.* **240**, 67-76 (2014).
25. Y. Qian, A. Panigrahy, C. M. Laymon, V. K. Lee, J. Drappatz, F. S. Lieberman, F. E. Boada, J. M. Mountz, Short- T_2 imaging for quantifying concentration of sodium (^{23}Na) of bi-exponential T2 relaxation. *Magn. Reson. Med.* **74**, 162-174 (2015).
26. P. M. Winter, N. Bansal, TmDOTP5—as a ^{23}Na shift reagent for the subcutaneously implanted 9L gliosarcoma in rats. *Magn. Reson. Med.* **45**, 436-442 (2001).
27. C. L. Lawson, R. J. Hanson, *Solving Least-Squares Problems* (Prentice Hall, Englewood Cliffs, 1974), Chapter 23, p.161.
28. G. H. Golub, C. F. Van Loan, *Matrix computations* (3rd Ed) (The John Hopkins University Press, Baltimore, ed. 3, 1996).
29. B. R. Kirkwood, J. A. C. Sterne, *Essential medical statistics* (Blackwell Science, Malden, 2003).

30. Y. Qian, T. Zhao, K. Lakshmanan, Y. Ge, Y. W. Lui, T. Shepherd, F. E. Boada, *Proof of concept for the separation of mono-T2 and bi-T2 sodium in human brain through two-TE acquisitions at 3T*, presented at the 25th Annual Meeting of the ISMRM, Honolulu, Hawaii, USA, 22-27 April 2017. p. 6355.
31. F. E. Boada, J. S. Gillen, G. X. Shen, S. Y. Chang, K. R. Thulborn, Fast three-dimensional sodium imaging. *Magn. Reson. Med.* **37**, 706-715 (1997).
32. K. Lakshmanan, R. Brown, G. Madelin, Y. Qian, F. Boada, G. C. Wiggins, An eight-channel sodium/proton coil for brain MRI at 3 T. *NMR Biomed.* **31**, e3867 (2018). [*NMR in Biomedicine*]
33. I. Goldstein, E. Lerer, E. Laiba, J. Mallet, M. Majaheed, C. Laurent, H. Rosen, R. P. Ebstein, D. Lichtstein, Association between sodium-and potassium-activated adenosine triphosphatase α isoforms and bipolar disorders. *Biological psychiatry.* **65**, 985-991 (2009).
34. A. F. Carvalho, J. Firth, E. Vieta, Bipolar disorder. *N. Engl. J. Med.* **383**, 58-66 (2020).
35. L. Xie, H. Kang, Q. Xu, M. J. Chen, Y. Liao, M. Thiagarajan, J. O'Donnell, D. J. Christensen, C. Nicholson, J. J. Iliff, T. Takano, Sleep drives metabolite clearance from the adult brain. *Science.* **342(6156)**, 373-377 (2013).
36. G. Madelin, R. Kline, R. Walvick, R. R. Regatte, A method for estimating intracellular sodium concentration and extracellular volume fraction in brain in vivo using sodium magnetic resonance imaging. *Sci. Rep.* **4**, 4763 (2014).
37. Y. Blunck, S. Josan, S. W. Taqdees, B. A. Moffat, R. J. Ordidge, J. O. Cleary, L. A. Johnston, 3D-multi-echo radial imaging of ^{23}Na (3D-MERINA) for time-efficient multi-parameter tissue compartment mapping. *Magn. Reson. Med.* **79**, 1950-1961 (2018).
38. J. M. Lommen, S. Flassbeck, N. G. Behl, S. Niesporek, P. Bachert, M. E. Ladd, A. M. Nagel, Probing the microscopic environment of ^{23}Na ions in brain tissue by MRI: on the accuracy of different sampling schemes for the determination of rapid, biexponential decay at low signal-to-noise ratio. *Magn. Reson. Med.* **80**, 571-584 (2018).
39. L. Leroi, A. Coste, L. de Rochefort, M. D. Santin, R. Valabregue, F. Mauconduit, E. Giacomini, M. Luong, E. Chazel, J. Valette, D. Le Bihan, Simultaneous multi-parametric mapping of total sodium concentration, T1, T2 and ADC at 7 T using a multi-contrast unbalanced SSFP. *Magn. Reson. Med.* **53**, 156-163 (2018).
40. A.A. Alhulail, P. Xia, X. Shen, M. Nichols, S. Volety, N. Farley, M. A. Thomas, A. M. Nagel, U. Dydak, U. E. Emir, Fast in vivo ^{23}Na imaging and mapping using accelerated 2D-FID UTE magnetic resonance spectroscopic imaging at 3 T: Proof of concept and reliability study. *Magn. Reson. Med.* **85**, 1783-1794 (2021).

41. B. Ridley, A. M. Nagel, M. Bydder, A. Maarouf, J. P. Stellmann, S. Gherib, J. Verneuil, P. Viout, M. Guye, J. P. Ranjeva, W. Zaaraoui, Distribution of brain sodium long and short relaxation times and concentrations: a multi-echo ultra-high field ^{23}Na MRI study. *Scientific reports*. **8**, 4357 (2018)
42. F. J. Kratzer, S. Flassbeck, S. Schmitter, T. Wilferth, A. W. Magill, B. R. Knowles, T. Platt, P. Bachert, M. E. Ladd, A. M. Nagel. 3D sodium (^{23}Na) magnetic resonance fingerprinting for time-efficient relaxometric mapping. *Magn. Reson. Med.* **86**, 2412-2425 (2021).
43. W. Syeda, Y. Blunck, S. Kolbe, J. O. Cleary, L. A. Johnston, A continuum of components: Flexible fast fraction mapping in sodium MRI. *Magn. Reson. Med.* **81**, 3854-3864 (2019).
44. F. Riemer, B. S. Solanky, C. A. Wheeler-Kingshott, X. Golay, Bi-exponential ^{23}Na T_2^* component analysis in the human brain. *NMR in Biomedicine*. **31**, e3899 (2018).
45. Y. Qian, A. A. Williams, C. R. Chu, F. E. Boada, Multi-component T_2^* mapping of knee cartilage with ultrashort echo time acquisitions: Ex vivo results. *Magn. Reson. Med.* **64**, 1427-1432 (2010).
46. Y. Qian, T. Zhao, G. C. Wiggins, L. L. Wald, H. Zheng, J. Weimer, F. E. Boada, Sodium imaging of human brain at 7 T with 15-channel array coil. *Magn. Reson. Med.* **68**, 1807-1814 (2012).
47. J. I. Jackson, C. H. Meyer, D. G. Nishimura, A. Macovski, Selection of a convolution function for Fourier inversion using gridding. *IEEE Trans. Med. Imaging*. **10**, 473-478 (1991).
48. R. D. Hoge, K. S. Kwan, G. B. Pike, Density compensation functions for spiral MRI. *Magn. Reson. Med.* **38**, 117-128 (1997).
49. P. B. Roemer, W. A. Edelstein, C. E. Hayes, S. P. Souza, O. M. Mueller, The NMR phased array. *Magn. Reson. Med.* **16**, 192-225 (1990).
50. S. Robinson, J. Jovicich. B_0 mapping with multi-channel RF coils at high field. *Magn. Reson. Med.* **66**, 976-988 (2011).
51. E. M. Haacke, R. W. Brown, M. R. Thompson, R. Venkatesan, *Magnetic resonance imaging - Physical principles and sequence design* (Wiley, New York, 1999).

Extended Data for
**Multi-TE Single-Quantum Sodium (^{23}Na) MRI: A Clinically Translatable
Technique for Separation of Mono- and Bi- T_2 Sodium Signals**

Yongxian Qian* *et al.*

*Corresponding author. Email: Yongxian.Qian@nyulangone.org

This PDF file includes:

Extended text, figures, and tables
Text
Figs. E1 to E6
Table (no)
References (no)

T_2^* values in whole brain of the study subjects

The MSQ approach needs an input of T_2^* values for mono- T_2 sodium, $T_{2,mo}^*$, and for bi- T_2 sodium, $T_{2,bs}^*$ and $T_{2,bl}^*$, at *each* voxel ΔV . Measurement of these values however is time consuming (~ 2 hours) and impractical in clinic routine. Alternatively, we use a global set of T_2^* values $\{T_{2,mo}^*, T_{2,bs}^*, T_{2,bl}^*\}$ for *all* voxels. This global set can be measured quickly (< 1 min) on whole brain of each study subject by acquiring free induction decay (FID) signal $s(t)$ and fitting it with multi-term exponential T_2^* decays to attain a T_2^* spectrum through Eq. (E1).

$$|s(t)| = \sum_j A_j \exp(-t/T_{2,j}^*) \quad (\text{E1})$$

Two representative FID signals and T_2^* spectra are illustrated in Fig. E1A for a healthy young subject (21 years old, male) and Fig. E1B for a patient with epilepsy (31 years old, male). The spectra are sparse with just 2–4 peaks, indicating that the global set of $\{T_{2,mo}^*, T_{2,bs}^*, T_{2,bl}^*\}$ is a reasonable estimate for the separation. Notably, these T_2^* values are different from subject to subject as shown in the two-dimensional (2D) scatter plot (Fig. E1C) from all 15 study subjects including nine healthy subjects and six patients. The short- T_2^* component is clearly crowded in a range of 1–5 ms while the long- T_2^* is widely scattered in three bands centered at 10, 20, and 30ms, respectively. Interestingly, the long- T_2^* component is shifted to lower values in the patient group, relative to the healthy group. There is no difference between males and females in the healthy group. Therefore, T_2^* values are heterogeneous across subjects and measurement of T_2^* spectrum is necessary for each subject.

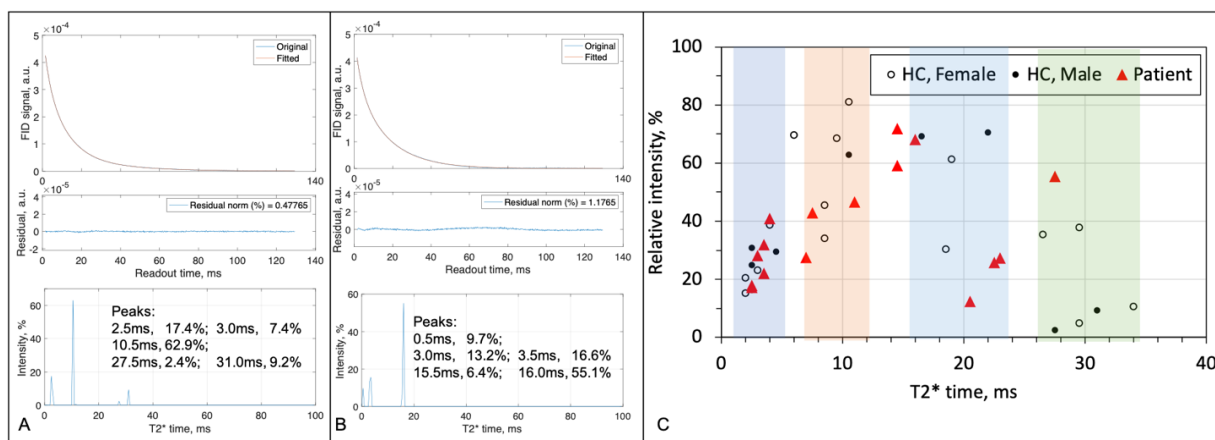


Fig. E1. Human study: 2D scatter plot of individual T_2^* components across all study subjects. (A) A typical T_2^* spectrum and associated FID signal and fitting error from whole brain of a healthy young subject (21 years old, male). **(B)** Another example from a patient with epilepsy (31 years old, male). **(C)** Scatter plot of individual T_2^* components.

Sensitivity of the separation to T_2^* values

What would happen for the separation if a global set of T_2^* values measured on whole brain is not the same as local one at a voxel? How sensitive the separation is to T_2^* values? Intuitively, the solution $\{m_{mo}, m_{bi}\}$ to Eq. (1) would not be very sensitive to T_2^* values due to exponential decays in Eqs. (1A, 1B). This observation can be verified theoretically and numerically.

Theoretically, small changes in T_2^* values, $\{\delta T_{2,q}^*, q=mo, bs, bl\}$, lead to small changes $\{\delta m_p, p=mo, bi\}$ in m_{mo} and m_{bi} under the same $m(t)$, that is,

$$0 = \delta(m_{mo}Y_{mo}) + \delta(m_{bi}Y_{bi}) \quad (E2)$$

$$-m_\delta = Y_{mo}\delta m_{mo} + Y_{bi}\delta m_{bi} \quad (E2A)$$

$$m_\delta \equiv m_{mo}\delta Y_{mo} + m_{bi}\delta Y_{bi} \quad (E2B)$$

$$\delta Y_q = \left(\frac{tY_q}{T_{2,q}^*}\right) \left(\frac{\delta T_{2,q}^*}{T_{2,q}^*}\right) \leq e^{-1} \left(\frac{\delta T_{2,q}^*}{T_{2,q}^*}\right), \quad q=mo, bs, bl \quad (E2C)$$

$$\delta Y_{bi} = a_{bs} \delta Y_{bs} + a_{bl} \delta Y_{bl} \leq e^{-1} \left[a_{bs} \left(\frac{\delta T_{2,bs}^*}{T_{2,bs}^*}\right) + a_{bl} \left(\frac{\delta T_{2,bl}^*}{T_{2,bl}^*}\right) \right] \quad (E2D)$$

Where δ is difference operator.

Numerically, errors in m_{mo} and m_{bi} can be calculated, given a series of $\{T_{2,q}^*, \delta T_{2,q}^*; q=mo, bs, bl\}$ at a specific pair (m_{mo}, m_{bi}) . This creates a plot showing how $\{m_{mo}, m_{bi}\}$ changes with $\{\delta T_{2,q}^*; q=mo, bs, bl\}$.

Fig. E2 shows two extreme cases: mono- T_2 sodium dominating at $m_{mo} = 0.9$ and bi- T_2 sodium dominating at $m_{bi} = 0.9$. In Fig. E2A, an error in $T_{2,mo}^*$ causes an error in m_{mo} or m_{bi} much smaller for the dominant one, e.g., $\delta m_{bi} < 2.2\%$ when $\delta T_{2,mo}^* < 20\%$, and $\delta m_{mo} < 2.9\%$ when $\delta T_{2,mo}^* < 5.0\%$. In Fig. E2B, an error in $T_{2,bs}^*$ has a small impact on both m_{mo} and m_{bi} , e.g., when dominating, $\delta m_{bi} < 4.8\%$ and $\delta m_{mo} < 0.04\%$ when $\delta T_{2,bs}^* < 20\%$. In Fig. E2C, an error in $T_{2,bl}^*$ leads to an error in m_{mo} or m_{bi} much smaller for the dominant one, e.g., $\delta m_{bi} < 5.2\%$ and $\delta m_{mo} < 0.6\%$ when $\delta T_{2,bl}^* < 20\%$. The best case is Fig. E2B where $T_{2,bs}^*$ has small impact ($< 4.9\%$) on both mono- and bi- T_2 sodium signals. The worst case is Fig. E2A (top) where $T_{2,mo}^*$ had a large impact on bi- T_2 sodium signal, $\delta m_{bi} = 35.6\%$ when $\delta T_{2,mo}^* = -5\%$. In other words, when the mono- T_2 sodium is very dominating, $T_{2,mo}^*$ value should be as accurate as possible (achievable via single- T_2^* map) to attain the best separation for the bi- T_2 sodium.

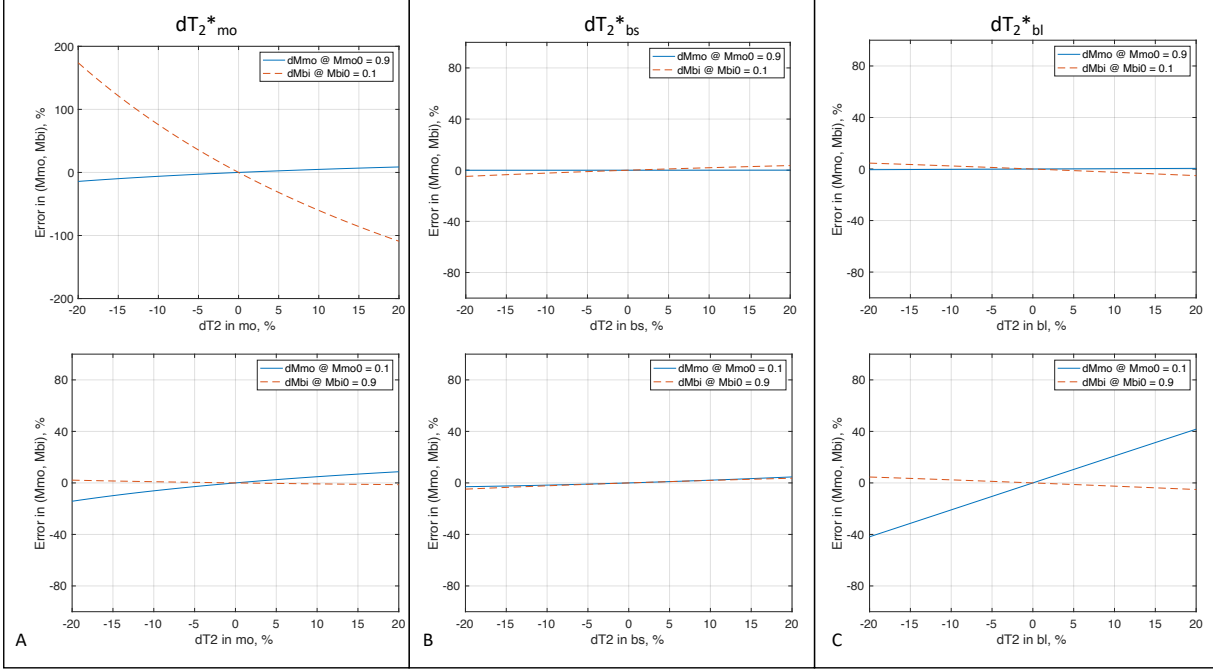


Fig. E2. Simulated impact of T_2^* values on separation of mono- and bi- T_2 sodium signals. The impact of individual T_2^* components on the separation of sodium signals (m_{mo} , m_{bi}) at $\{T_2^*_{mo}, T_2^*_{bs}, T_2^*_{bl}\} = (50.0, 3.5, 15.0)$ ms for two extreme cases: mono- T_2 sodium dominating (top row), $m_{mo}=0.9$, and bi- T_2 sodium dominating (bottom row), $m_{bi}=0.9$. **(A)** An error in $T_2^*_{mo}$ produces an error in m_{mo} or m_{bi} much smaller for the dominant signal. **(B)** An error in $T_2^*_{bs}$ has a small impact on both m_{mo} and m_{bi} . **(C)** An error in $T_2^*_{bl}$ leads to an error in m_{mo} or m_{bi} much smaller for the dominant one. The best case is Column B where the $T_2^*_{bs}$ had small impact ($<4.9\%$) on both mono- T_2 and bi- T_2 sodium signals. The worst case is (A) where the $T_2^*_{mo}$ had a large impact on the bi- T_2 sodium signal, $\Delta m_{bi} = 35.6\%$ when $\Delta T_2^*_{mo} = -5\%$.

Optimization of the number of TEs

In principle, the more TEs the better differentiation between T_2^* relaxations of the mono- and bi- T_2 sodium populations. In practice, the number of TEs is restricted by total scan time (TA), SNR, signal decay, and risk of motion across TEs. Therefore, a trade-off must be made for the number of TEs. To determine an optimal number of TEs, it is necessary to understand noise propagation in Eq. (2). We applied singular value decomposition (SVD) analysis (28) on matrix \mathbf{Y} in Eq. (2), i.e.,

$$\mathbf{Y} = \mathbf{U} \mathbf{\Sigma} \mathbf{V}^T \quad (\text{E3})$$

$$\mathbf{\Sigma} = \text{diag}(\sigma_1, \sigma_2) \quad (\text{E3A})$$

$$\mathbf{X} = \mathbf{V} \mathbf{\Sigma}^{-1} \mathbf{U}^T \mathbf{M} \quad (\text{E3B})$$

Singular values ($\sigma_1 \geq \sigma_2 \geq 0$) determine noise transfer (amplification or suppression) in Eq. (E3C) from the measured TE-images \mathbf{M} to the separated mono- and bi- T_2 sodium images \mathbf{X} . However, Eq. (E3B) allows negative values in \mathbf{X} when random noise contaminates \mathbf{M} . This violates the “non-negative” condition on \mathbf{X} . Therefore, the SVD analysis is applicable only to \mathbf{X} elements with $\text{SNR} \geq 2$ where the elements, with Gaussian noise, have 95.4% of chance in the territory of non-negative value (29).

Fig. E3 presents the results at a typical set of T_2^* values, $\{T_{2,mo}^*, T_{2,bs}^*, T_{2,bl}^*\} = \{50.0, 3.5, 15.0\}$ ms for three cases of interest: an ideal case of 80 TEs, practical case #1 of 8 TEs, and practical case #2 of two TEs. Singular value σ_2 is less than 1.0 for the 8-TE and 2-TE cases, leading to an amplification of noise. Therefore, a better choice for less noise amplification is the 2-TE case, in

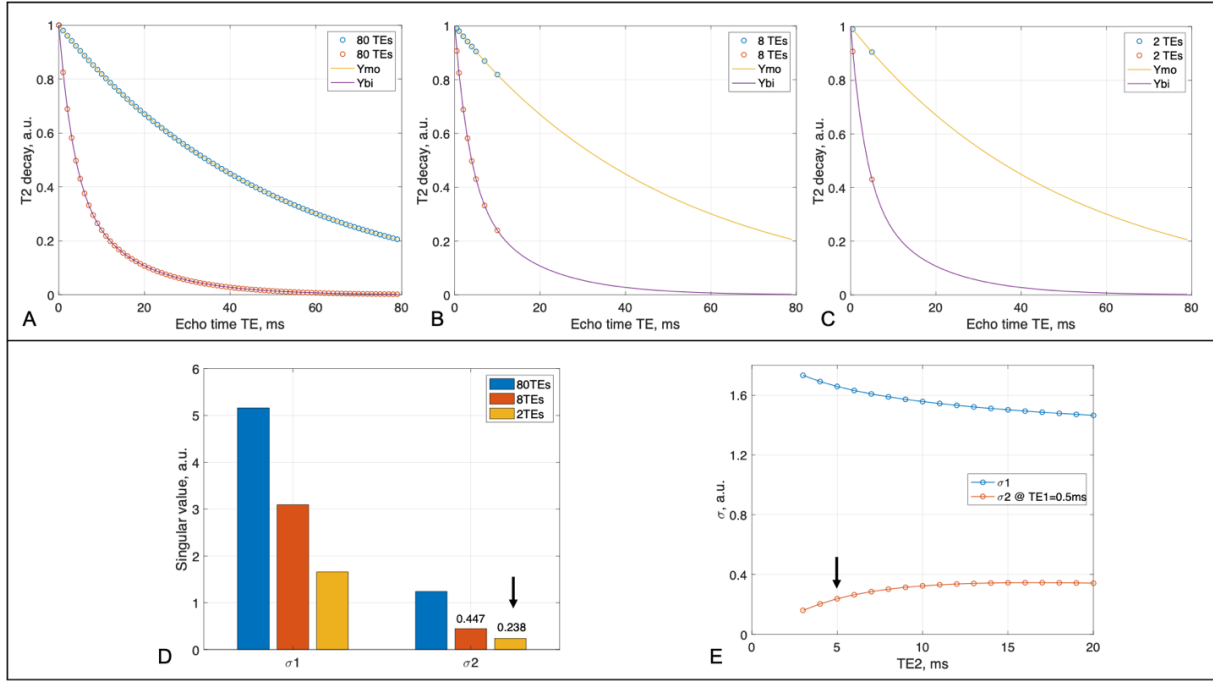


Fig. E3. Optimization of TE sampling scheme via SVD analysis. (A) A reference sampling scheme of 80 TEs in a range of 0–79 ms at an interval of 1.0ms, distributing on a mono-exponential T_2^* decay Y_{mo} (TE) of mono- T_2 sodium at a typical value of $T_{2,mo}^* = 50$ ms, and on a bi-exponential T_2^* decay Y_{bi} (TE) of bi- T_2 sodium at a typical set $\{T_{2,bs}^*, T_{2,bl}^*\} = \{3.5, 15.0\}$ ms. (B) An intuitively-favorable scheme of 8 TEs at $\{0.5, 1, 2, 3, 4, 5, 7, 10\}$ ms, distributing on the decay curves Y_{mo} and Y_{bi} . (C) The optimal scheme of 2 TEs at $\{0.5, 5\}$ ms. (D) SVD singular values (σ_1 and σ_2) of the three TE sampling schemes. (E) Singular values of the 2-TE scheme changing with the 2nd TE (or TE₂). In D, σ_2 is less than 1.0 at the 8-TEs and 2-TEs, leading to noise amplification. Thus, a better choice for less noise amplification is the 2-TEs (arrow). In E, TE₂ at 5ms (arrow) produced a value near maximum for σ_2 while preserving higher signal than the larger TE₂. Therefore, the 2-TEs scheme is an optimal one for the human brain.

which TE₂ at 5ms produced a value near maximum of σ_2 while preserving higher signal than larger TE₂. Thus, the 2-TE scheme was selected for human studies.

Numerical simulations

The separation of mono- and bi-T₂ sodium signals was first investigated on numerical models via Eq. (3) at a typical set of T₂^{*} values, (T_{2,mo}^{*}, T_{2,bs}^{*}, T_{2,bl}^{*}) = (50.0, 3.5, 15.0) ms, and an optimal two-TE scheme, TE = (0.5, 5.0) ms. Sodium image signals were calculated via Eq. (1), with an additive Gaussian noise, $N(0, \sigma^2)$, at each of noise trials (independent from each other), $m(t) + n(t)$. The mono- and bi-T₂ signal intensities { m_{mo} , m_{bi} } vary in a normalized range of 0.1–0.9 at a step size = 0.1. The separation was implemented using the function *lsqnonneg*() in MATLAB, and repeated N_{noise} times at each of the specific intensity. Mean and standard deviation (SD) were reported as the separated sodium signal. $N_{noise}=1054$ was chosen to detect a 10% of SD, or 0.1 effect size $d=\Delta\mu/SD$, in difference between the mean and true value at 90% power and 5% significant level under the two-sided Student's *t*-test (29).

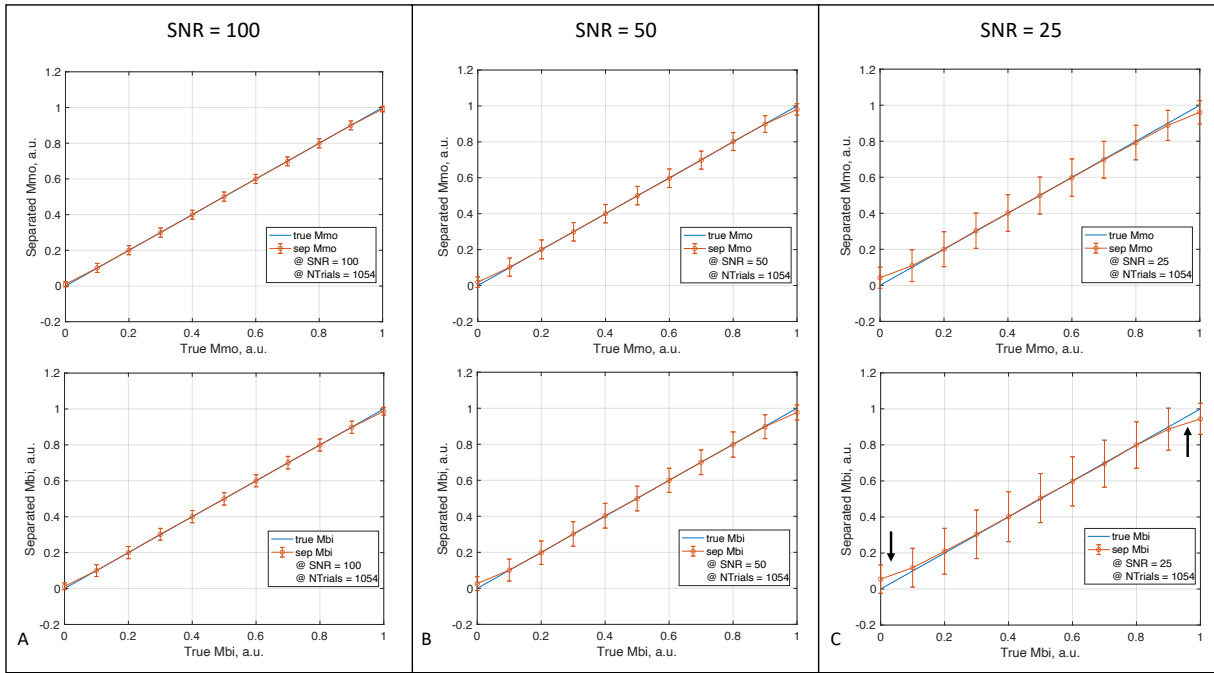


Fig. E4. Simulated separation of the mono- and bi-T₂ sodium signals. Sodium signals (m_{mo} , m_{bi}) were simulated at a typical set of (T_{2,mo}^{*}, T_{2,bs}^{*}, T_{2,bl}^{*}) = (50.0, 3.5, 15.0) ms and the 2-TE scheme TE=(0.5, 5.0). (A) Extra-high SNR = 100. (B) High SNR = 50. (C) Regular SNR = 25. The standard deviation (error bar) of the separated m_{mo} (top row) and m_{bi} (bottom row) consistently decreased with SNR increasing from 25 to 100. There was an underestimate (3.9–5.6%, arrow) for m_{mo} or m_{bi} near maximum value 1.0, but an overestimate (4.2–5.5%, arrow) near minimum value 0.0, with an amount decreasing with SNR increasing.

Fig. E4 demonstrates the simulated separation at three SNRs of interest: 100 (extra-high), 50 (high), and 25 (regular). The SD (error bar) consistently decreased with SNR increasing. There was an underestimate in m_{mo} and m_{bi} near maximum value 1.0, but an overestimate near minimum value 0.0 with an amount decreasing with SNR increasing.

Phantom studies

The separation was then investigated on four phantoms with known sodium concentrations, which were custom-built and described in previous work (25, 30). The phantoms are 50-mL centrifuge tubes filled with a mixture of distilled water, 10% w/w agar powder, and sodium chloride (NaCl) at three concentrations of 90, 120, and 150 mM and at 150mM without agar, to mimic bi- and mono- T_2 sodium signals in human brains. Sodium MRI was performed on a clinical scanner at 3T (MAGNETOM Trio Tim, Siemens Medical Solutions, Erlangen, Germany) with a dual-tuned (^1H - ^{23}Na) volume head coil (Advanced Imaging Research, Cleveland, OH). The data acquisition was

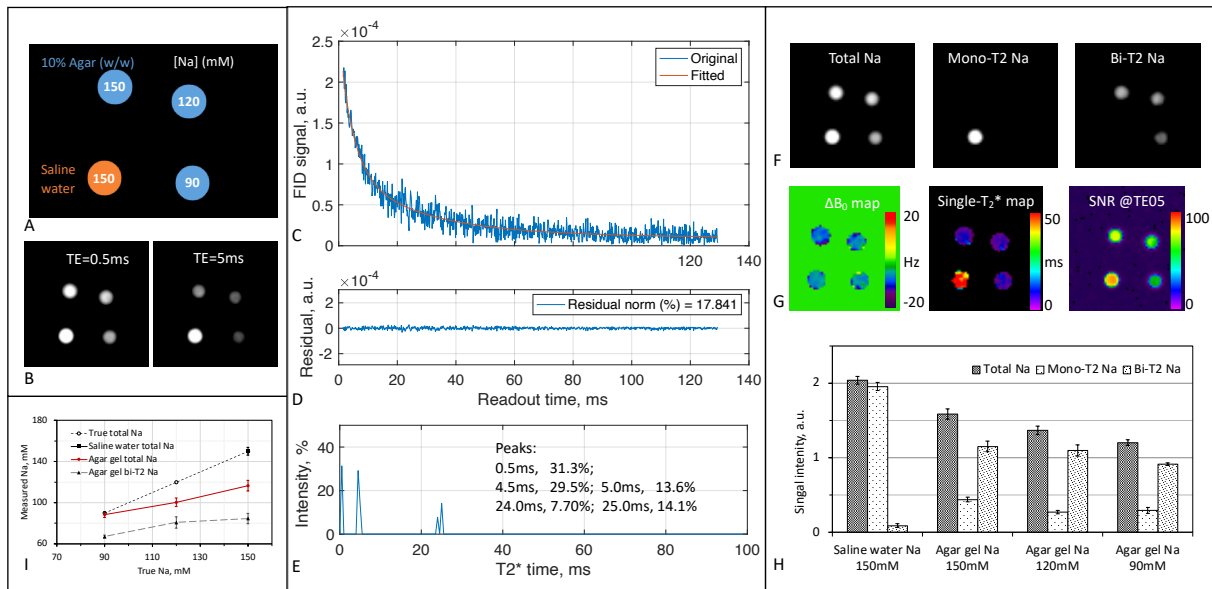


Fig. E5. Phantom study. (A) Phantoms of four tubes with sodium concentration: 150mM for the saline water (simulating mono- T_2 sodium ions) and 90, 120, 150 mM for the agar gels (simulating bi- T_2 sodium ions). (B) Sodium images of the phantoms at TE₁/TE₂=0.5/5ms, shown in the same window/level. (C) FID signals (original and fitted) from the four tubes (no averaging), with the correction for distortion at the first five data points. (D) Residual error of the fitting in C. (E) T_2^* spectrum calculated from FID in C and used to produce the fitted FID. (F) Sodium images (total, mono- T_2 , and bi- T_2) separated from the two images in B at (T_{2*mo} , T_{2*bs} , T_{2*bl}) = (50, 5, 25) ms according to E and G. (G) Maps of ΔB_0 and single- T_2^* calculated from the images in B, and a map of SNR at TE=0.5ms. (H) Separated sodium signals in the regions of tubes in F. (I) Quantified sodium concentration from F.

implemented using an SNR-efficient, three-dimensional (3D) pulse sequence called twisted projection imaging (TPI) (31).

Fig. E5 summarizes outcomes of the phantom studies (30). Fig. E5A shows phantom arrangement of the four tubes and Fig. E5B are sodium images at $TE_1/TE_2=0.5/5\text{ms}$. Figs. E5C-E demonstrates FID signal from all the four tubes at averages=1, residual fitting error, and T_2^* spectrum. Fig. E5F includes the sodium images separated at $(T_{2,mo}^*, T_{2,bs}^*, T_{2,bl}^*) = (50, 5, 25)$ ms according to T_2^* spectrum in Fig. E5E. The maps of ΔB_0 , single- T_2^* , and SNR are in Fig. E5G. Signal intensity of the separated sodium signals (mean \pm SD) in the tubes is in Fig. E5H and the quantification of sodium concentration is in Fig. E5I. The separation in Fig. E5H recovered 95.8% of mono- T_2 sodium signal in the saline water tube, while leaving 4.2% to bi- T_2 sodium signal, much better than 20% left by the subtraction approach (25). The separation recovered 72.5, 80.4, and 75.9 % of bi- T_2 sodium signal in the agar tubes at sodium concentrations of 150, 120, and 90mM, respectively. The quantification of sodium concentration in Fig. E5I, when calibrated at the saline water, showed a systematic bias in total and bi- T_2 sodium concentrations, leading to an underestimate of sodium concentrations.

Validation via the estimates of upper-limit for extra- and intracellular volume fractions

Different from the phantom studies above, where ground truth of sodium concentrations is known, the human studies lack the ground truth for validation. Although each step in the MSQ separation is scientifically reasonable and its outcome should be believed correct, we alternatively and indirectly validate it by applying the separated sodium images to estimation of the upper-limit of extra- and intracellular volume fractions for which accurate measurements are available in literatures (8, 26, 35, 36). We assigned all mono- T_2 sodium to extracellular space and all bi- T_2 sodium to intracellular space, although they may co-exist in both extra- and intracellular spaces. The estimates (mean and SD) were made in ROIs of gray matter (GM) and white matter (WM) across three continuous slices via Eqs. (E4–E6) using sodium concentrations $C_{ex}=145\text{mM}$ for extracellular space and $C_{in}=15\text{mM}$ for intracellular space.

$$v_{ex} = 1/(1 + a) \quad (\text{E4})$$

$$v_{in} = a/(1 + a) \quad (\text{E5})$$

$$a = m_{bi}C_{ex}/m_{mo}C_{in} \quad (\text{E6})$$

Fig. E6 presents these upper-limit estimates in the healthy group and shows significant ($P=0.023$) difference in volume fraction between the gray and white matters: 89.6 ± 4.5 vs. 94.0 ± 2.6 % for intracellular space, in line with the literature values of 75 vs. 92 % (8, 26); and 10.4 ± 4.5 vs. 6.0 ± 2.6 % for extracellular space, comparable to literature values of 14.1 ± 1.8 (35) vs. 18 ± 5 % (36).

No significant difference ($P=0.953$) was found between the healthy and patient groups ($N=9$ and 6 , respectively).

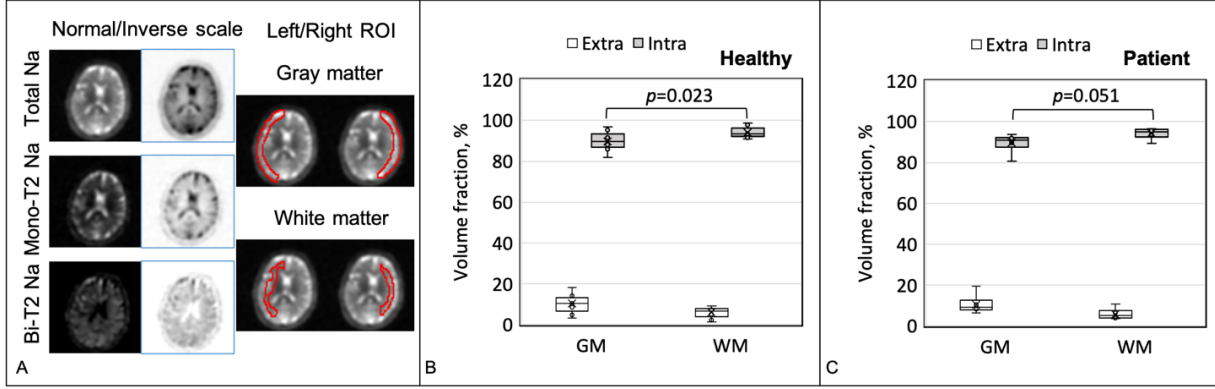


Fig. E6. Estimates of upper-limit of the volume fraction for extra- and intracellular spaces. (A) Typical sodium images (total, mono- T_2 , and bi- T_2) and regions of interest (ROIs) for the gray matter (GM) and white matter (WM) in an axial slice from a healthy subject. **(B)** Volume fractions for the healthy group ($N=9$). **(C)** Volume fractions for the patient group ($N=6$). **Note:** difference in volume fraction is statistically significant between the gray and white matters ($P=0.023$) for the healthy group, but not for the patient group ($P=0.051$). No significant difference was observed between the healthy and patient groups for gray or white matter ($P=0.953$).

Calculation of the separation sensitivity to T_2^* values

We used the most common set of T_2^* values in our human studies, $\{T_{2,mo}^*, T_{2,bs}^*, T_{2,bl}^*\} = \{50.0, 3.5, 15.0\}$ ms, as true values, and calculate via Eqs. (1–3) the separation error $\{\delta m_{mo}, \delta m_{bi}\}$ relative to the ground truth of mono- and bi- T_2 sodium signals $\{m_{mo}, m_{bi}\}$ when adding errors $\delta T_{2,q}^*$, $q=mo, bs, bl$, up to $\pm 20\%$ to the true T_2^* values. The relationship between $\{\delta T_{2,q}^*; q=mo, bs, bl\}$ and $\{\delta m_{mo}, \delta m_{bi}\}$ was plotted out in Extended Data Fig. E2. To focus on the relation of “ $\delta T_2^* - \delta m$ ”, TEs were sampled in an ideal case with $TE_0 = 0$, $\Delta TE = 1.0$ ms, and 80 TEs covering entire T_2^* decays.

Calculation for optimal number of TEs

The calculations were implemented via Eq. (6) for three cases: an ideal case serving as reference, practical case #1 having a large number of TEs, and practical case #2 having a small number of TEs. The ideal case has 80 TEs, i.e., $TE = 0, 1, 2, \dots, 79$ ms, to cover entire range of T_2^* decays. The two practical cases, suggested by existing human studies (25, 31, 45, 46) and being the most sensitive to T_2^* decays (45), were investigated under the constraint of total scan time (TA) = 22 min.

The practical case #1 has 8 TEs, i.e., TE = 0.5, 1, 2, 3, 4, 5, 7, and 10ms; and the practical case #2 only has two TEs, i.e., TE = 0.5 and 5.0ms with 4 averages for each TE.

Numerical simulation

These simulations were performed in MATLAB on the MacBook Pro laptop or Windows desktop, otherwise specified. Random noise of Gaussian distribution was generated using MATLAB function *randn(n)*, while the NNLS algorithm was implemented using $[x, resnorm, residual] = lsqnonneg(C, d)$.

Phantom experiments

We custom-built four phantoms, which were detailed in our previous work (25). The phantoms are 50-mL centrifuge tubes filled with a mixture of distilled water, 10% w/w agar powder, and sodium chloride (NaCl) at three concentrations (90, 120, and 150 mM) and at 150mM without agar, mimicking bi- and mono-T₂ sodium signals in brain tissues. MRI data acquisition was implemented using an SNR-efficient, three-dimensional (3D) pulse sequence called twisted projection imaging (TPI) (31), with parameters: rectangular RF pulse duration = 0.8ms, flip angle=80° (limited by SAR and TR), field of view (FOV)=220mm, matrix size=64, nominal resolution=3.44mm (3D isotropic), TPI readout time=36.32ms, total TPI projections=1596, TPI *p*-factor=0.4, TR=100ms, TE₁/TE₂=0.5/5ms, averages=4, and TA=10.64min per TE-image. The sodium images were offline reconstructed on a desktop computer (OptiPlex 7050, 8GB memory, Windows 10, DELL, Round Rock, TX) using the gridding algorithm (47, 48) and a custom-developed programs in C++ (MS Visual Studio 2012, Microsoft, Redmond, WA). The mono- and bi-T₂ sodium signals was separated using a custom-developed program as described above.

Supplementary Information for
**Multi-TE Single-Quantum Sodium (^{23}Na) MRI: A Clinically Translatable
Technique for Separation of Mono- and Bi- T_2 Sodium Signals**

Yongxian Qian* *et al.*

*Corresponding author. Email: Yongxian.Qian@nyulangone.org

This PDF file includes:

Supplementary Text
Figs. S1 to S5
References (no)

Extrapolation of N-term exponential decay

We once accidentally read a reference in literature about this topic, but could not find the citation at hand, thus summarize here the algorithm in our own language, specifically for the recovery of FID signals. If a signal $f(t)$ is an N -term exponential decay as defined in Eq. (S1) with parameters $\{A_i, b_i; i = 1, 2, \dots, N\}$, and is sampled at a uniform interval Δt , then a sample $f(t_0)$ at time t_0 can be represented by a linear combination of its late-time neighboring samples $\{f(t_0 + j\Delta t), j = 1, 2, \dots, M\}$, as shown in Eq. (S2), with coefficients $\{a_j, j = 1, 2, \dots, M \geq N\}$ to be determined.

$$f(t) = \sum_{i=1}^N A_i e^{-t \cdot b_i} \quad (\text{S1})$$

$$f(t_0) = \sum_{j=1}^M a_j f(t_0 + j\Delta t) \quad (\text{S2})$$

Proof. Extending $f(t_0 + j\Delta t)$ in Eq. (S2) according Eq. (S1) gives

$$\begin{aligned} f(t_0) &= \sum_{j=1}^M a_j \left[\sum_{i=1}^N (A_i e^{-t_0 \cdot b_i}) (e^{-j\Delta t \cdot b_i}) \right] \\ &= \sum_{i=1}^N A_i e^{-t_0 \cdot b_i} \left(\sum_{j=1}^M a_j e^{-j\Delta t \cdot b_i} \right). \end{aligned} \quad (\text{S3})$$

Select time-invariant coefficients $\{a_j, j = 1, 2, \dots, M > N\}$ to satisfy Eq. (S4), thus Eq. (S2) holds.

$$\sum_{j=1}^M a_j e^{-j\Delta t \cdot b_i} = 1, \text{ for } i = 1, 2, \dots, N. \quad (\text{S4})$$

Note. The descriptions above are for backward extrapolation in time and used in the recovery of FID signal. The forward extrapolation also holds if Δt is replaced with $-\Delta t$ in Eqs. (S2–S4). To find the unknown coefficients $\{a_j, j = 1, 2, \dots, M\}$, Eq. (S2), instead of Eq. (S4), is usually used on such a segment of $f(t)$ that it is not distorted and involves all the N exponential decays. The number of data samples on the segment should be larger than M to form an over-determined problem in case of random noise existing in the signal $f(t)$.

Correction for hardware-related distortion of FID signal

Fig. S1 demonstrates a FID signal from a healthy subject (52 years old, male), with and without correction for the distortion at the first five ADC samples using Eq. (S2) with $(M, N) = (5, 3)$. The correction removed distortion and reduced overall residual fitting error from 2.33% to 1.49%. The correction also improved resolution of short- T_2^* components: from singlet at 2.5ms to doublet at 0.5ms and 2.5ms (Figs. S1A3, B3).

Calculation stability of T_2^* spectrum at a high resolution of $\Delta T_2^* = 0.5\text{ms}$

T_2^* spectrum was calculated via Eq. (4) on an FID signal using an established algorithm – non-negative least squares (NNLS) – at a high spectral resolution of $\Delta T_2^* = 0.5\text{ms}$ in a range of 0.5–100ms. Such a high resolution raises a concern on stability of the calculation as the base functions

at these spectral locations, $\exp(-t/T_2^*)$, are not independent from each other. To address this concern, we employed singular value decomposition (SVD) to analyze the transfer matrix \mathbf{E} , and used numerical simulation to detail the impact of random noise on the T_2^* spectrum.

The SVD analysis on the transfer matrix \mathbf{E} are as the follows.

$$E_{i,j} \equiv \exp(-t_i/T_{2,j}^*), \quad i = 1, 2, \dots, N, \quad j = 1, 2, \dots, M, \quad N \gg M \quad (\text{S5A})$$

$$\mathbf{E}^T \mathbf{E} = \mathbf{U} \mathbf{\Sigma} \mathbf{V}^T \quad (\text{S5B})$$

$$\mathbf{\Sigma} = \text{diag}(\sigma_1, \sigma_2, \dots, \sigma_M) \quad (\text{S5C})$$

with sampling time $t_i = TE + (i - 1) * \Delta t$ and spectral location $T_{2,j}^* = j * \Delta T_2^*$. Singular values $\{\sigma_j, j = 1, 2, \dots, M\}$ determine stability of the calculation for T_2^* spectrum in terms of random noise interference in Eq. (4). Correlation coefficients between the base functions are also calculated.

$$R_{j1,j2} = (E^T E)_{j1,j2} / \sqrt{(E^T E)_{j1,j1} (E^T E)_{j2,j2}}, \quad j1, j2 = 1, 2, \dots, M \quad (\text{S6})$$

At $\Delta t = 0.05\text{ms}$, $TE=0.2\text{ms}$ and $N=2048$, the singular values and correlation coefficients were calculated and shown in Fig. S2. The singular value σ quickly decreases to zero ($<10^{-10}$) at index (15, 13, 10, 9) when ΔT_2^* increases from 0.5ms to 1.0, 3.0 and 5.0ms, respectively. This indicates the existence of null subspace or multiple solutions for T_2^* spectrum (Fig. S2, top). The normalized correlation coefficients R between any two T_2^* base functions is spreading out from diagonal line, confirming non-orthogonal between the base functions (Fig.S2, bottom). However, the extent of spreading is narrower for short T_2^* values at high resolution $\Delta T_2^* = 0.5\text{ms}$ than at low resolution $\Delta T_2^* = 5\text{ms}$.

Numerical simulation for the impact of random noise on the T_2^* spectrum was performed at three popular components, $T_2^*=3, 15$, and 50ms with relative amplitudes $A=30, 20$, and 50 , respectively, plus an additive normal random noise generated by function $\text{randn}(n, l)$, at $\text{SNR} \equiv f(t=0)/\text{SD} = 100, 50$, and 25 . Outcomes of the simulations were summarized in Fig. S3, where peak parameters at doublets (Fig. S3, bottom) were linearly combined with amplitude-weighting by left- and right-peaklets in Eq. (S7). The best spectrum was achieved at $\text{SNR}=100$ among the three noisy cases, relative to no noise.

$$T_2^* = (A_L * T_{2,L}^* + A_R * T_{2,R}^*) / A \quad (\text{S7A})$$

$$A = A_L + A_R \quad (\text{S7B})$$

Measurement stability of FID signals on whole brain: B_0 shimming

The B_0 shimming may change from subject to subject in routine practice, leading to a concern on measurement stability of the FID signals, thus the T_2^* spectra, from whole brain across subjects. This concern is addressable because sodium (^{23}Na) MRI has about 4-fold lower resonance frequency than proton (^1H) MRI (e.g., 33.8 vs. 127.7 MHz at 3T), and the manual shimming (three iterations) is better than auto shimming. Fig. S4 shows the results of all 15 subjects studied, with a small standard deviation (SD) in whole-brain histograms. There was no significant difference between the healthy and patient groups ($P=0.908$). Thus, the manual shimming, or ΔB_0 , is stable.

Invisibility of CSF T_2^* peaks in the spectrum: single T_2^* mapping

Cerebrospinal fluid (CSF) in the brain is known to have a T_2^* value of $\sim 50\text{ms}$ as seen in single- T_2^* maps (Figs. 7, 8). But this sodium population was not observed in the T_2^* spectra. This phenomenon might be caused by small volume of CSF relative to whole brain. To confirm this cause, Fig. S5 presents two representative whole-brain histograms of single- T_2^* mapping, with very small numbers of voxels (invisible bins) for CSF at $T_2^* \sim 50\text{ms}$.

Fig. S1. FID signal and T_2^* spectrum with and without correction.

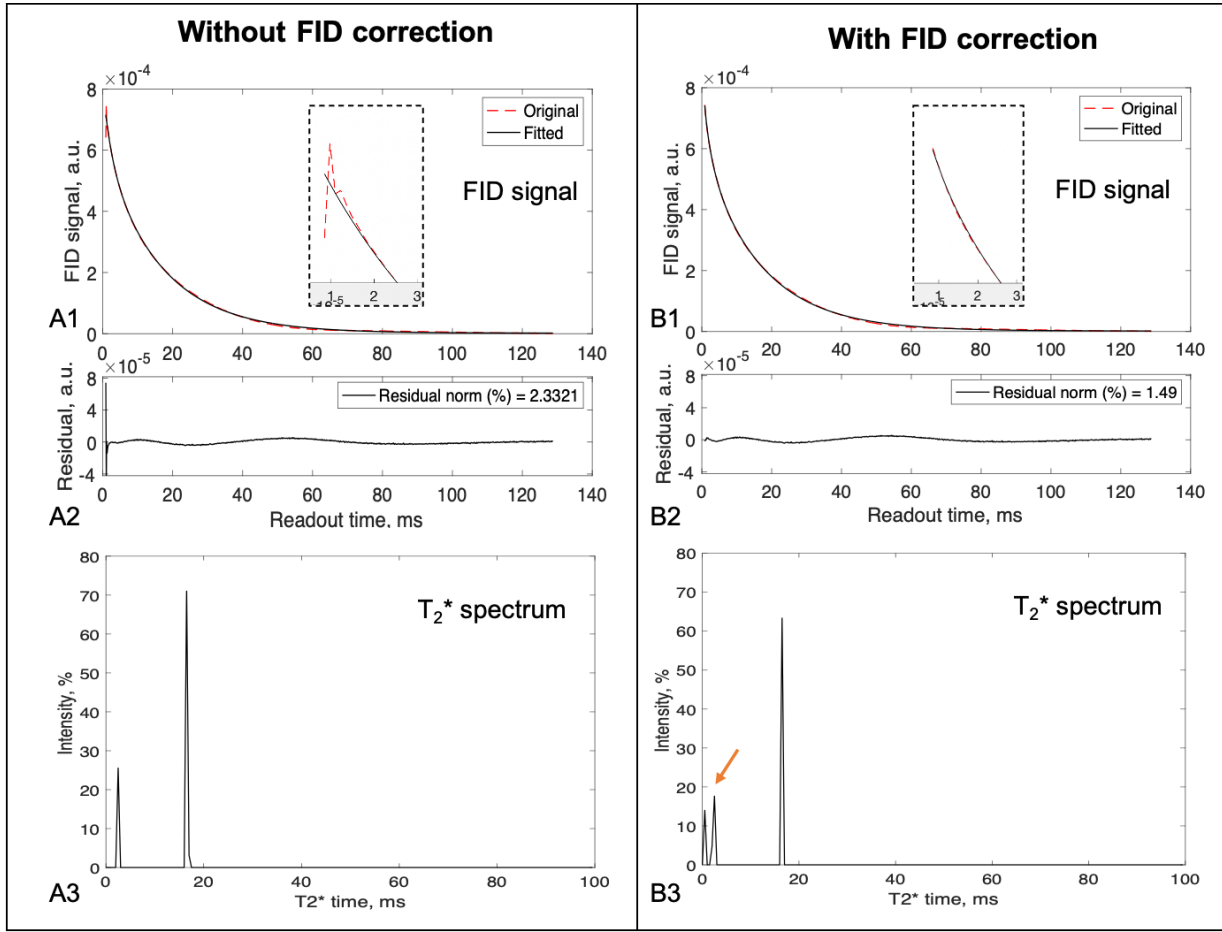


Fig. S1. FID signals (top) and T_2^* spectra (bottom) from whole brain of a healthy subject (52 years old, male), with (Fig. S1B) and without (Fig. S1A) correction for FID distortion at the first five samples shown in the insets. In the middle are residual errors from the fitting using the T_2^* spectra in the bottom. The FID correction removed the distortion, significantly reduced residual error, and clearly improved resolution of short- T_2^* components from singlet at 2.5ms to doublet at 0.5ms and 2.5ms as well as peaks' intensity (Fig. S1B3). Data acquisition: 3T scanner (Prisma, Siemens) with a custom-built dual-tuned (^1H - ^{23}Na) 8-channel head array coil (32), *fid* sequence, rectangular RF duration=0.5ms, TE/TR=0.35/300ms, averages=128, ADC samples=1024 at an interval of 0.125ms.

Fig. S2. Calculation stability of T_2^* spectrum.

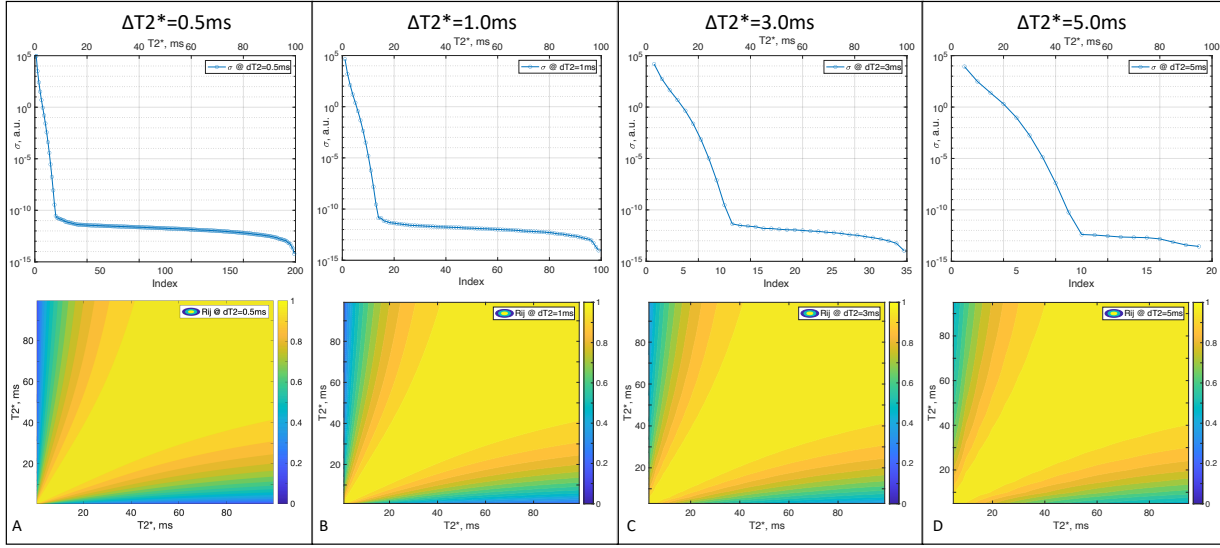


Fig. S2. The SVD singular values of matrix $E^T E$ (top) and correlation coefficients of the base-in matrix E (bottom). (A) – (D) T_2^* spectral resolution at $\Delta T_2^* = 0.5, 1.0, 3.0$, and 5.0 ms. In the top, singular value σ quickly decreases to zero ($<10^{-10}$) at index (15, 13, 10, 9) respectively, indicating the existence of null subspace or multiple solutions for the T_2^* spectrum. In the bottom, the normalized correlation coefficient $R_{j1,j2}$ between any two T_2^* base functions $\exp(-t/T_{2,j}^*)$ is spreading out from diagonal line, showing non-orthogonal between the base functions.

Fig. S3. Numerical simulation for the impact of random noise on T_2^* spectrum.

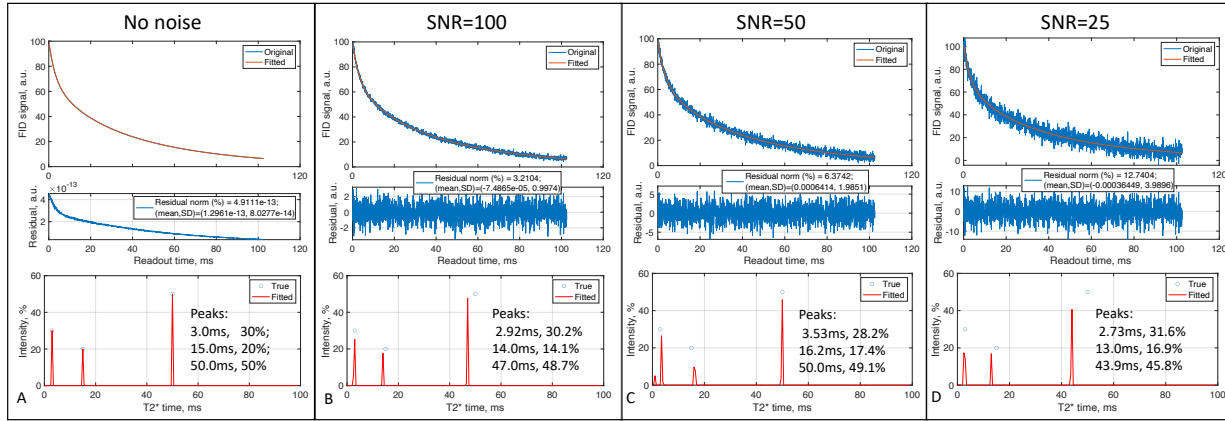


Fig. S3. Calculation stability of T_2^* spectrum using the algorithm NNLS via MATLAB function $lsqnonneg(C,d)$ and the numerical simulations at three popular components: $T_2^*=(3, 15, 50)$ ms with relative amplitudes $A=(30, 20, 50)$ plus an additive random noise generated by function $randn(n,1)$. (A) – (D) are the simulations at $\Delta T_2^* = 0.5$ ms with noise at three typical values SNR = 100, 50, and 25. The peak parameters at doublets (bottom) were linearly combined with amplitude-weighting (Eq. S7). The best spectrum was achieved at SNR=100 among the three noisy cases.

Fig. S4. Measurement stability of FID signals on whole brain: B_0 shimming

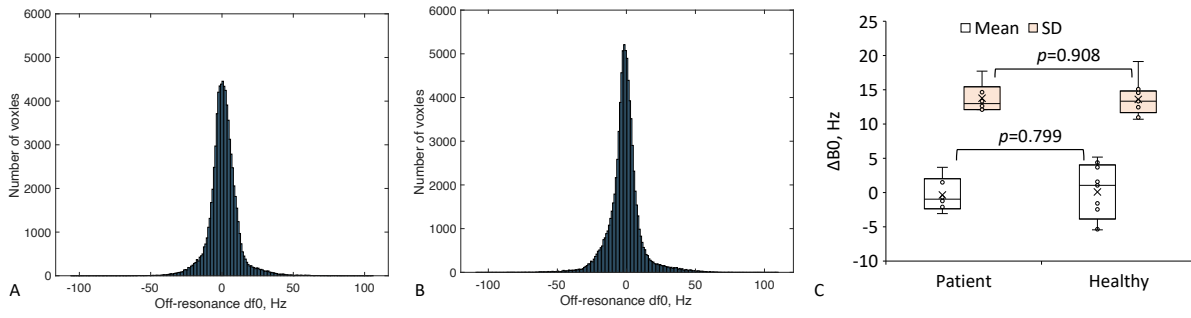


Fig. S4. Whole brain histograms of ΔB_0 mapping at $TE_1/TE_2 = 0.5/5$ ms under a manual shimming procedure (3 iterations). **(A)** A representative histogram from a healthy subject (52 years old, male), with $\text{mean} \pm \text{SD} = 1.0 \pm 10.7$ Hz. **(B)** Another example from a patient with epilepsy (31 years old, male), with $\text{mean} \pm \text{SD} = -1.2 \pm 12.1$ Hz. **(C)** Mean and SD distribution of whole-brain ΔB_0 histograms from all 15 study subjects including 9 healthy and 6 patients, showing no significant difference between the two groups (healthy vs. patient), $P = 0.799$ for the mean and $P = 0.908$ for the SD.

Fig. S5. Invisibility of CSF T_2^* peak in the spectrum: single T_2^* mapping.

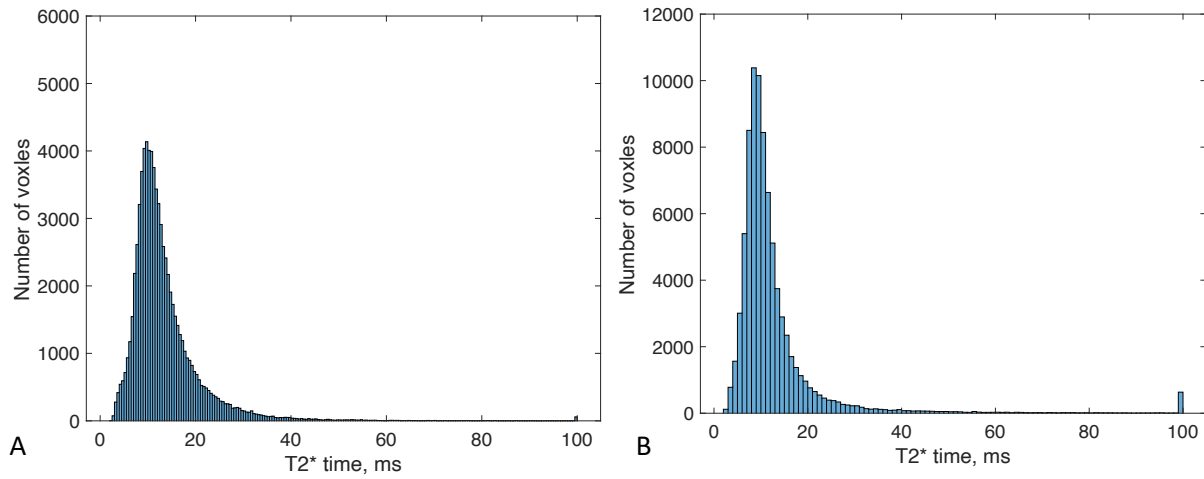


Fig. S5. Representative whole-brain histograms of single- T_2^* mapping at $TE_1/TE_2 = 0.5/5$ ms. **(A)** A healthy subject (52 years old, male). **(B)** An epilepsy patient (31 years old, male). These, as well as the other healthy subjects and patients we studied, showed very small numbers (invisible bins) of voxels for CSF at $T_2^* \sim 50$ ms. Note: a visible bin at $T_2^* = 100$ ms counts voxels of T_2^* values ≥ 100 ms.